NCC1-11

Final Technical Report

A Radiative Transfer Model for Remote Sensing of Laser Induced Fluorescence of Phytoplankton in Non-homogeneous Turbid Water

NASA - Cooperative Agreement

1983

Principal Investigator
D. D. Venable
Hampton Institute
Hampton, VA

Technical Monitor and Cooperative Investigator
L. R. Poole
NASA LaRC
Hampton, VA

Table of Contents

Preface

This final technical report consists of three documents organized into three chapters.

The first chapter is entitled "A Semi-Analytic Monte Carlo Radiative Transfer Model for Oceanographic Lidar Systems". This chapter summarizes the computer model SALMON as it was developed for homogeneous media. It discusses the advantages of the model over more conventional Monte Carlo techniques used by other researchers. Chapter 1 served as a preliminary version for a paper published by L. R. Poole, D. D. Venable and J. W. Campbell.

The second chapter is entitled "Sensitivity of Airborne Fluorosensor Measurements to Linear Vertical Gradients in Chlorophyll Concentrations". This chapter gives detailed discussions on the application of the stratified model to useful measurement related problem. Much of the material introduced in chapter 2 is expanded in chapter 3. This chapter serves as a preliminary paper for proposed publication.

The final chapter is entitled "SALMON Modifications for Non-homogeneous Media". This chapter discusses the extension utilized to make the SALMON code appliable to stratified media. Some comparisons of the stratified and homogeneous models are discussed.

In addition to the work presented here, several papers have been published by L. R. Poole et. al. concerning SALMON. The results contained in these reports were developed collaboratively by D. D. Venable, L. R. Poole, J. W. Campbell and A. R. Punjabi.

Chapter 1

A Semianalytic Monte Carlo Radiative Transfer Model for Oceanographic Lidar Systems

L. R. Poole, D. D. Venable and J. W. Campbell

Much attention has been focused recently on the application of lidar techniques to oceanographic research problems (ref. 1), particularly those of interest to biological oceanographers. Variations in time and space of important biological parameters present a formidable obstacle for the researcher using conventional shipboard sampling and measurement techniques. Measurements made using shipboard or towed lidar systems, such as the proposed Submerged LIDAR and SONAR (SLAS) system, would enhance conventional measurements, but would still be faced with the problems associated with spatial and temporal variability. However, it is felt that carefully planned integration of precise, but localized shipboard measurements with less precise, but synoptic measurements made using lidar remote-sensing techniques from aircraft or helicopters could lead to a much greater understanding of important research areas such as, for example, phytoplankton ecology (ref. 2). In addition, such a combination of measurements could serve as a surface-truth benchmark calibration of any future satellite-borne remote sensors addressing the same problems.

Presently, oceanographic lidar measurements are, at best, semi-empirical in that only a rudimentary understanding exists of the effects of a number of factors (i.e.: attenuation of the laser beam in the water medium -diffuse or beam attenuation, or vertical inhomogeneities in the medium). A technique is needed for investigating the accuracy of LIDAR system measurements over a wide range of environmental conditions, as well as for various boundary conditions and source/sensor geometric configurations. This letter presents a semi-analytic Monte Carlo radiative transfer simulation model (SALMON) which is particularly well suited for addressing these fundamental questions. Sample results are presented which highlight the advantage of using SALMON as opposed to purely stochastic Monte Carlo techniques.

Monte Carlo simulation techniques have been used rather extensively in recent years to study radiative transfer in the atmosphere and oceans. In its simplest digital form, a Monte Carlo model is a purely stochastic construction of an ensemble of photon trajectories through the medium of interest, with the length and direction of each trajectory segment governed by probability density functions derived from the basic scattering and absorption properties of the medium. In most applications, some technique or combination of techniques for reducing the variance in the computed results is used in order to obtain meaningful results at a reasonable computer cost. Examples of Monte Carlo studies of oceanic radiative transfer can be found in Plass and Kattawar (ref. 3), Funk (ref. 4), Gordon et al. (ref. 5), and Thomas and Guenther (ref. 6). The last of these examines, for the case of an unlimited field-of-view receiver, the influence of scattering and absorption mechanisms on the performance of a bathymetric lidar system, one which infers water depth in coastal regions by transmitting a laser pulse into the water and monitoring the return pulse from the water-bottom interface. Thomas and Guenther state that a topic of major interest not included in their results is the quantitative effect of a limited receiver field of view.

An obvious technique for limiting the receiver field of view in a Monte Carlo simulation of any lidar remote-sensing system is to accept as "successful" only those photon trajectories which terminate at a point lying within a predefined receiver aperture (at some height above the air-water interface) and whose final segment is in a direction lying within the confines of a specified angular field of view (see fig. 1). For most physical systems, the true geometric constraints are very restrictive, and, as a result, the probability of "success" for any given photon trajectory is very small. The only choices

available to the researcher using a purely stochastic approach are to construct a very large ensemble of trajectories, thereby consuming considerable computer resources, or to relax the geometric constraints to more practical values and compute an average value of the detected signal over a much broader field of view than that associated with the actual sensor.

A semi-analytic approach, however, one in which the detector signal is evaluated through a combination of stochastic and analytic techniques, offers an effective means for modeling the lidar system with realistic geometric constraints. The approach used in developing SALMON is frequently called the "method of expected values" or the "method of statistical estimation" (ref. 7). Consider again figure 1; suppose that the $j^{\underline{th}}$ segment of a photon trajectory constructed using standard Monte Carlo methodology is in direction $\vec{\xi}$ and terminates at some point $\vec{q}$ within the "interaction volume", that volume enclosed by an extension into the water (with refraction effects) of the cone defining the detector field-of-view.

At this point in its history, we can conceive of the photon as representing a large number of photons, each traveling in the same direction and having the same amount of energy (the sum of which equals the energy level of the true photon at point $\vec{q}$). With a knowledge of the probability density functions governing photon motion, we can estimate the fraction of this large number of photons which, after interacting with, say, a sediment particle at point $\vec{q}$, (1) will scatter through an angle θ' toward a direction $\vec{\xi}'$ which lies within the small solid angle $\Delta\Omega$ subtended by the detector aperture A_{ap} at point $\vec{q}$, and (2) will proceed from point $\vec{q}$ to the aperture without further interaction with the medium (or with the atmosphere, should we have to consider its effects, also). Neglecting atmospheric effects, the estimate, or expected value, of the fraction of photons collected by the remote receiver

upon a scattering event at point $\vec{q}$ can be written as

$$E = \frac{p(\theta')}{4\pi} \Delta\Omega \, e^{-cd} \, T_s \qquad (1)$$

where $p(\theta')$ is the scattering phase function (assumed constant over the small solid angle $\Delta\Omega$), which gives the rate at which energy is scattered into an element of solid angle $\Delta\Omega$ about direction θ' (ref. 8). The term e^{-cd} is the probability that the photons scattered through angle θ' will then transmit from point $\vec{q}$ to the air-water interface (a distance d') with no further interactions. The term c is of course the beam attenuation coefficient for the water medium and T_s is the Fresnel transmittance of the air-water interface. An analogous relationship can be written for fluorescent emission from a chlorophyll-bearing particulate, with the scattering phase function replaced by a function characterizing the angular emission pattern of the particulate (usually assumed to be isotropic). Upon each scattering event (or fluorescent emission) occurring within the interaction volume, the expected value of the energy reaching the detector is recorded, and the total energy of the fraction remaining at point $\vec{q}$ is reduced by the same expected value. The length and direction of the $j+1$ st trajectory segment are then selected using standard probability density functions, except in the case in which the new segment is in a direction toward the air-water interface. In such instances, the segment length is drawn from a distribution which is truncated (ref. 9) to ensure that the photon will remain within the water medium and potentially contribute again to the cumulative detector signal. SALMON also makes use of the statistical weighting technique (ref. 9) whereby photons are prevented from being absorbed by the water

molecules themselves (and thus removed from the field), but rather allowed to proceed to further interactions, with an appropriate adjustment in energy level.

To check the validity of SALMON, sample results were compared with those obtained using a Monte Carlo model incorporating the statistical estimation methodology of Plass and Kattawar (ref. 9) (PKM). If a photon is traveling directly toward a given detector (counting bin) after any interaction with the water medium, PKM estimates and records the flux expected to reach that detector as a function of the optical distance along the current photon path to the detector. Sample cases were constructed in which photons at an incident wavelength λ = 450 nm were injected at normal incidence at an identical spatial location (zero beam spread) into an infinitely deep homogeneous water medium whose sole constituent was 1.7×10^7 cells/ml of a common blue-green algae (Anacystis marinus). Atmospheric effects were ignored and the air/water interface was assumed to be perfectly flat. Both SALMON and PKM were executed in a dual mode in which photons can be detected not only via single and multiple scattering by the algal cells at the incident wavelength, but also via absorption by the chloroplasts contained in the cells and subsequent fluorescent emission, with a reduced energy level, at λ = 685 nm, the primary fluorescent wavelength of chlorophyll a. These fluoresced photons at λ = 685 nm are then susceptible to scattering and absorption by other algal cells. Scattering and absorption coefficients for the algal medium were measured using the cadre of instruments described in Whitlock et al. (ref. 10) and are listed in Table 1 for the two wavelengths under investigation. Absorption coefficients for pure water were obtained from Smith and Tyler (ref. 11) while the fluorescence efficiency η

(the ratio of photons fluoresced to photons absorbed by an algal cell) at λ = 450 nm was estimated by combining the measured absorption coefficient with data provided by Farmer (ref. 12). (Second-order fluorescence was assumed negligible; hence η for λ = 685 nm was set equal to zero.) The test medium was purposely chosen to be optically thick to maximize the number of photon interactions within the medium, and thus to provide a reasonable upper limit for the computational time required to execute the models. However, SALMON is by no means restricted to optically thick media.

For the test cases, it was assumed that scattering at both wavelengths, and fluorescent emission at λ = 685 nm, were isotropic. For the PKM model, the estimated flux exiting the medium within a radius of 1 meter from the entry point of the incident photons was collected in 10 polar-angle counting bins (of equal solid angle) ranging up to a maximum emergent polar angle of 8.1 degrees from zenith. For SALMON, a hypothetical detector geometry was defined as an analog to the innermost collecting bin of PKM, which recorded the flux exiting (within a 1-meter radius) at polar angles less than 2.56 degrees from zenith. This innermost bin was found to be the smallest practical "detector" field-of-view which would yield results having an acceptable variance at a reasonable computer cost using PKM, but is still an order of magnitude larger than the field-of-view commonly associated with LIDAR system detectors.

Comparative normalized histograms of detected signals at λ = 685 nm for the test cases using SALMON and PKM are shown in figure 2. The SALMON histogram shows the distribution of sample means of 20 independent sets of 1000 photon trajectories. The PKM histogram stemmed from 36 independent sets of 10^4 photon trajectories; however, since isotropic scattering and emission were specified in the test cases, it was found that the exiting radiance distribution was nearly uniform with polar angle, and it was thus assumed that each of the

10 counting bins could be treated as an independent collector. Thus, the PKM histogram shows the distribution of 360 sample mean detected signals, rather than just the 36 collected in the innermost bin. Even though the overall mean estimated signal is nearly the same for the models, figure 2 shows that the variance in the estimate of the overall mean made using SALMON is only a small fraction of that experienced using PKM. In addition, construction of the 36×10^4 photon trajectories using PKM required 15 times the computer resources (executing in FORTRAN Extended Version 4 on a CDC CYBER 175 computer at the Langley Research Center) expended in construction of the 20000 SALMON trajectories. Similar results were obtained for $\lambda = 450$ nm, but are not shown in the interest of brevity.

To further illustrate the utility of SALMON, it was executed again for the same optical medium, with the exception of substitution of the spectral average of the sharply anisotropic measured scattering phase functions for Anacystis marinus (fig. 3) to govern scattering events at both $\lambda = 450$ nm and $\lambda = 685$ nm. In this case, the remote detector was defined as having a horizontally oriented circular aperture of area .05 cm^2 at an altitude of 150 m, with the field of view limited to 6.67 milliradians from the vertical (resulting in a 1-m radius footprint at the surface). This configuration is a realistic model for helicopter-borne LIDAR remote-sensing system geometries. SALMON was executed in Extended Basic on the Hampton Institute PDP 11/34 computer system in sets of 1000 photon trajectories and the cumulative average detector signal (total signal/total number of trajectories) was computed at the conclusion of each set. Figure 4 shows a history of the convergence of the cumulative average signal for both wavelengths. Fluctuation in the cumulative average signal for each wavelength is within ± 3 percent after only 30,000 trajectories,

which required approximately 7.5 hours for execution on the PDP 11/34 and approximately 1 minute for execution on the CDC Cyber 175. Preliminary results obtained using SALMON with much lower concentrations of Anacystis marinus (1.7×10^5 to 1.7×10^6 cells/ml) show convergence histories quite similar to those in figure 4. Execution time required for these optically thinner cases was somewhat less than that required for the optically thick case due to fewer photon interactions within the interaction volume.

This letter has presented a semi-analytic Monte Carlo simulation methodology (SALMON), which is particularly well suited for addressing fundamental radiative transfer problems in oceanographic LIDAR, and gives a framework for investigating the effects of a host of environmental factors on LIDAR system performance. For the test cases shown, which include both isotropic and anisotropic scattering and isotropic fluorescent emission, SALMON provides minimal variance, rapidly convergent estimates of detected signals for a physically realistic remote sensor geometry. Preliminary results for optically thinner media indicate that performance similar to that shown for optically thick media can be expected with SALMON, at a somewhat reduced level of computational time.

The authors wish to thank Dr. Wayne Esaias for many hours of fruitful discussion, and Mr. David Christilf for invaluable support in computer program translation. We also wish to acknowledge Dr. George Kattawar for inspiring the original thoughts leading up to the development of SALMON.

REFERENCES

1. Carder, K. R.: Report on Oceanic Lidar Workshop Held at GSFC, Greenbelt, Maryland, November 13-14, 1980. NASA Technical Memorandum, In Press.

2. Esaias, W. E.: Remote Sensing of Oceanic Phytoplankton: Present Capabilities and Future Goals. Primary Productivity in the Sea, P. G. Falkowski, ed., Plenum Press, New York, 1980.

3. Plass, G. N. and Kattawar, G. W.: Appl. Opt. 8, 1969, p. 455.

4. Funk, C. J.: App. Opt. 12, 1973, p. 301.

5. Gordon, H. R.; Brown, O. B.; and Jacobs, M. M.: Appl. Opt. 14, 1975, p. 417.

6. Thomas, R. W. L. and Guenther, G. C.: Proceedings, Int. Conf. on Lasers, Orlando, Florida, December 1[illegible]. pp. 48-59, STS Press, McLean, Virginia, 1979.

7. Spanier, J. and Gelbard, E. M.: Monte Carlo Principles and Neutron Transport Problems. Addison-Wesley Publishing Co., Reading, Massachusetts, 1969.

8. Smith, R. C.; Austin, R. W.; and Petzold, T. J.: Volume Scattering Functions in Ocean Waters. Suspended Solids in Water, R. J. Gibbs, ed., Plenum Press, New York, 1974.

9. Plass, G. N. and Kattawar, G. W.: J. Atmos. Sciences 28, 1971, p. 1187.

10. Whitlock, C. H. et al. Appl. Opt. 20, 1981, p. 517.

11. Smith, R. and Tyler, J.: Transmission of Solar Radiation into Natural Waters. Photochemical and Photobiological Reviews, Vol. 1., K. Smith, ed., Plenum Press, New York, 1976.

12. Farmer, F. H.: NASA-Langley Research Center, unpublished data.

FIGURE CAPTIONS

Figure 1. - Remote-sensing geometric model.

Figure 2. - Normalized histograms of sample mean detector signal using SALMON and PKM.

Figure 3. - Spectrally averaged scattering phase function for blue-green algae.

Figure 4. - Convergence history of cumulative average detector signal using SALMON.

TABLE 1 - Optical Properties of Test Medium

	λ = 450 nm	λ = 685 nm
Total beam attenuation coefficient, m^{-1}	16.01	8.20
Scattering coefficient for algae, m^{-1}	13.70	7.00
Absorption coefficient for algae, m^{-1}	2.28	0.75
Absorption coefficient for water, m^{-1}	0.03	0.45
Fluorescence efficiency	0.00254	0.0

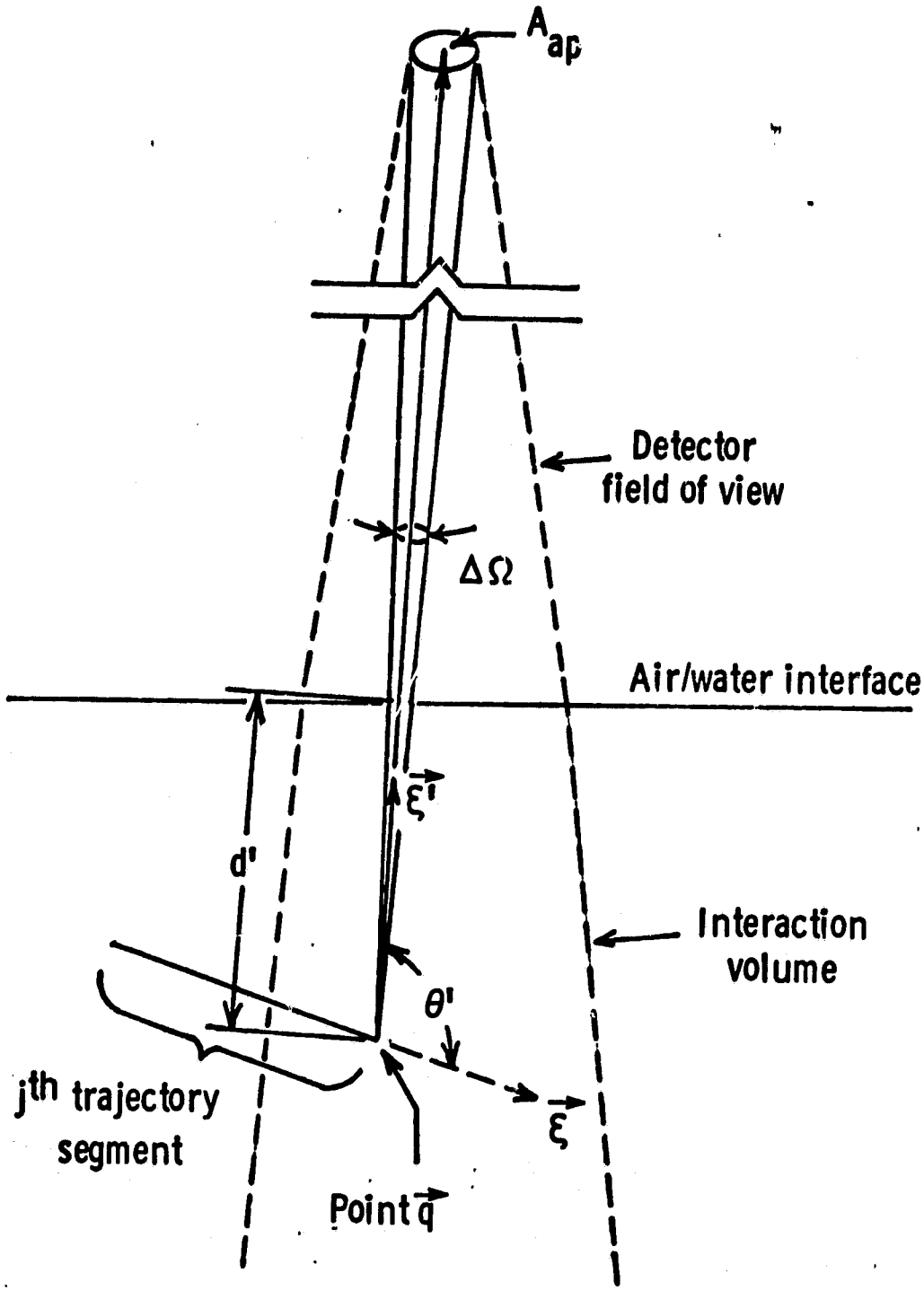

Figure 1. - Remote sensing geometric model.

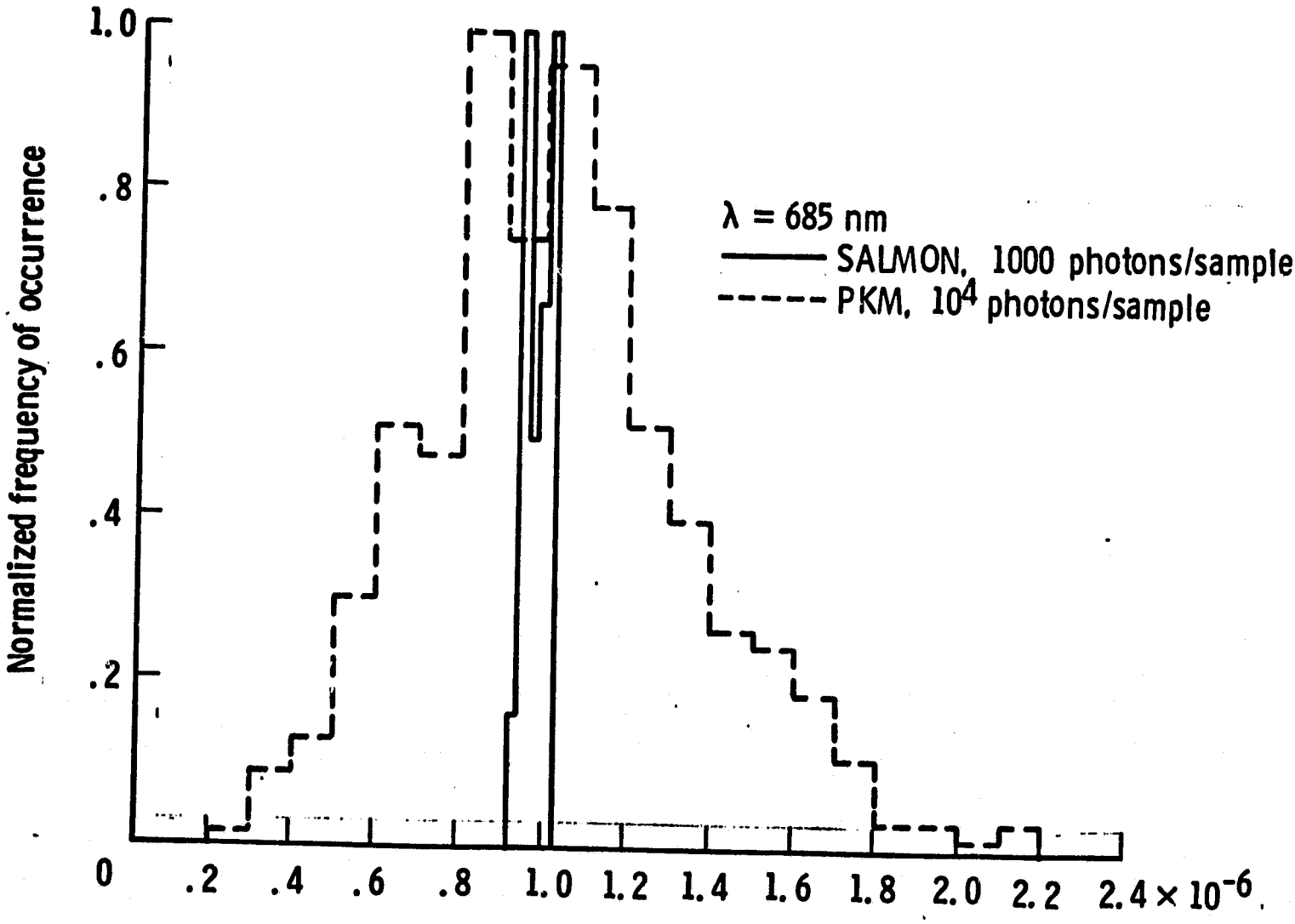

Figure 2. - Normalized histograms of sample mean detector signal using SALMON and PKM.

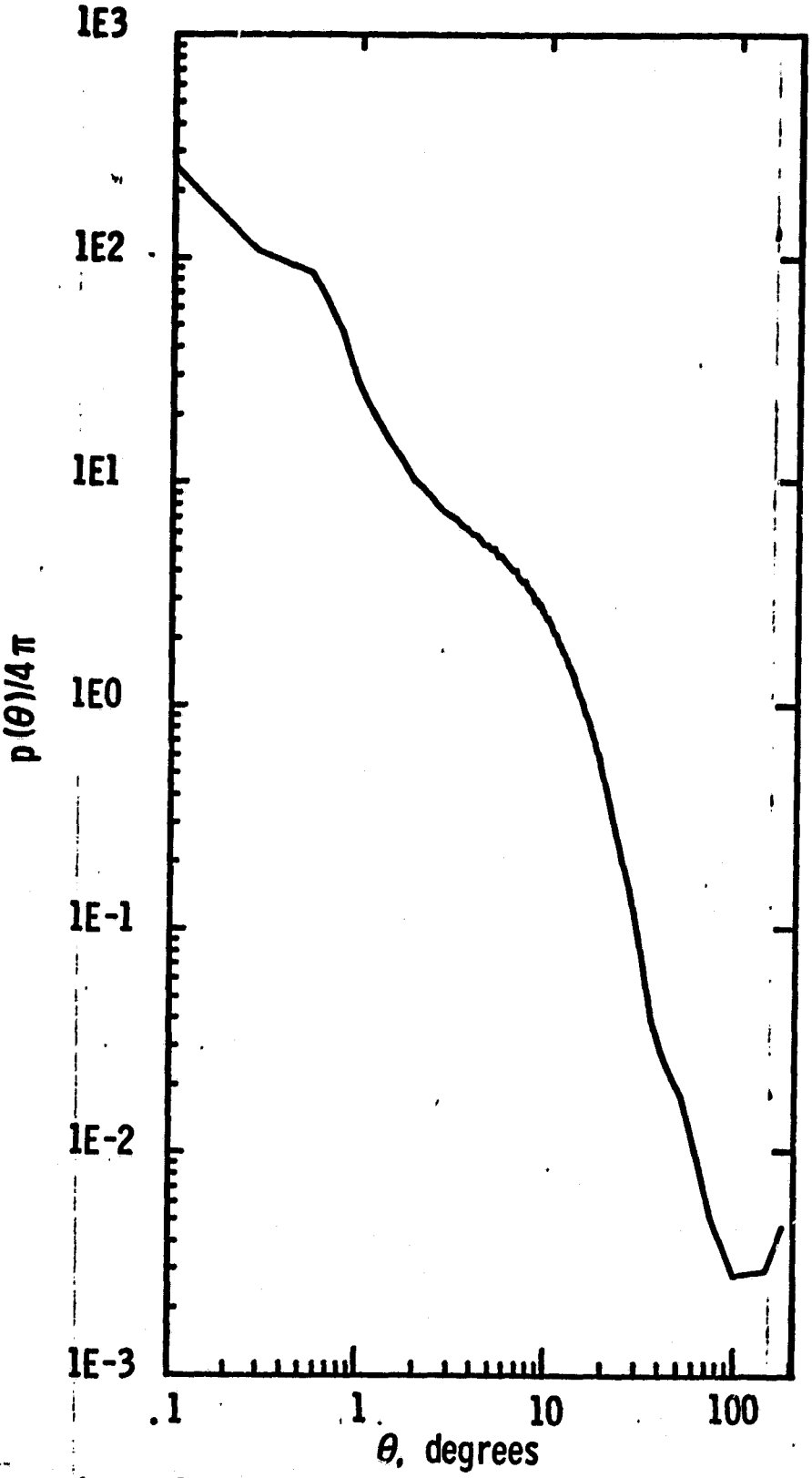

Figure 3. - Spectrally averaged scattering phase function for blue-green algae.

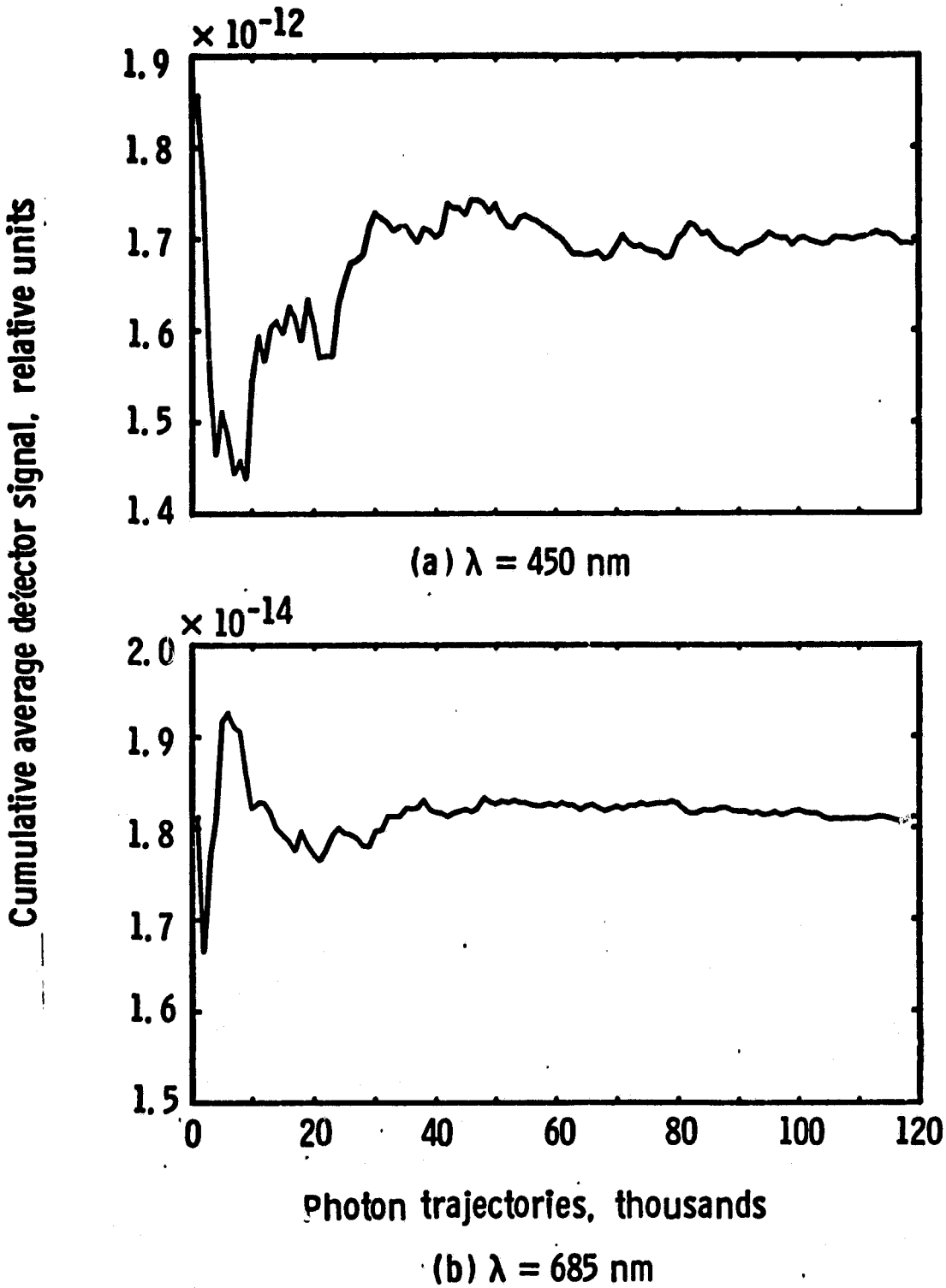

Figure 4. - Convergence history of cumulative average detector signal using SALMON.

Chapter 2

Sensitivity of Airborne Fluorosensor Measurements to Linear Vertical Gradients in Chlorophyll Concentrations

D. D. Venable, A. R. Punjabi and L. R. Poole

Introduction

We employ a semianalytic Monte Carlo radiative transfer model (SALMON)[1,2] to investigate the effects of vertical inhomogeneities in phytoplankton concentration in clear sea water on airborne laser-induced signals due to chlorophyll fluorescence and water Raman scattering. In this model, the detector signal is evaluated through a combination of stochastic and analytic techniques making it possible to model lidar systems with realistic geometric constraints and at the same time reduce required computer resources.

A layered approach is used to characterize changes in phytoplankton concentration, and thus optical parameters, as a function of depth. This approach allows media to be represented by combinations of homogeneous layers of various thicknesses. We assume that appropriate optical parameters can be defined for, and that horizontal homogeneity holds within each layer.

The geometry of the physical set-up used in the model is shown in Fig. 1. The geometric model is the same used in previous studies[1,2] except that the medium is divided into 21 layers, where layer 1 is always the atmosphere. The clear water medium, containing chlorophyll is divided into 20 layers. The concentration of chlorophyll in each layer must remain constant, but concentrations may vary from layer to layer. Our current modeling effort considers only linear variations in concentration and assumes that the airborne laser platform is at an altitude sufficiently low that atmospheric effects can be neglected.

In Fig. 1, $\vec{q}$ is the termination point of the j^{th} trajectory of the photon packet, $\vec{\xi}$ is the direction of propogation of the packet, and θ' is the angle through which photons must be scattered at point $\vec{q}$ in order to be collected by the detector within the solid angle $\Delta\Omega$. A_{ap} is the area of the detector aperature and the detector is located at the laser source, 150m above the

water surface. The detectors field of view and the interaction volume are represented by broken lines in the figure. The distances d_2, d_3, . . . refer to the distances that a photon packet must travel through layer 2, layer 3, . . . to reach the surface, assuming it had scattered through an angle θ' at point $\vec{q}$. The refractive index of the water medium is assumed to be the same for each layer. Thus, no refractions occur at the boundaries within the medium.

Each layer thickness may be set to any desired value. Thicknesses were selected so that for a given surface concentration, the depth of the bottom of layer 20 is approximately two to three times the maximum signal-integrated depth, $Z_{90,max}$, obtained from homogeneous results for the three wavelengths involved. The values we used for $Z_{90,max}$ were taken from Ref. 3 for homogeneous concentrations that were the same as the surface concentrations used in the layered model. The signal depth, Z_{90}, is that value above which 90% of the total signal observed at the detector originates.[3] The thickness of the 21st layer is set to a large enough value that photons do not reach the bottom of the medium. Optical properties for each layer are based on the layer's chlorophyll concentration. The concentration for the medium can be denoted by C(z), where z is depth in the medium. The downward direction is taken to be positive and the surface concentration is given by C_o. The gradient is defined to be, g, where

$$g = \frac{1}{C_o} \frac{dC(z)}{dz} \tag{1}$$

and is given in units of m^{-1}. In the layered model, the concentration assigned to the k^{th} layer is the averaged values of C(z) at the top and bottom of the layer. Concentration in the 21st layer is assigned so that the difference in concentrations for the 21st and 20th layers is the same as the difference in concentrations for the 20th and 19th layers. Computations for negative gradients of -10% m^{-1}, -15% m^{-1}, and -20% m^{-1} were not made for

surface concentrations less than 1 μg/l, since, in these cases the concentration of chlorophyll would reach zero at a depth less than $Z_{90,max}$. These concentration profiles would thus deviate from the linearly varying case and could not be compared to other cases considered in the simulation.

Special consideration must be given when the photon packet crosses the interface between two layers.[4] For example, consider the case where the photon packet travels from layer k to layer k ± 1. We select the distance the photon packet travels, δ_k, from an appropriate distribution function.[5] The value of δ_k is the distance the photon packet would travel in a homogeneous media, that is, if the packet remained in the k^{th} layer. However, if a layer boundary is crossed, the additional distance that the photon packet travels in layer k ± 1 is given by

$$\delta_{k \pm 1} = (\delta_k - \delta_k') \frac{\alpha_T^k}{\alpha_T^{k \pm 1}} , \qquad (2)$$

where δ_k' is the actual distance traveled in layer k and α_T^k and $\alpha_T^{k \pm 1}$ are the total attenuation coefficients in layers k and k ± 1, respectively.

In this study, the common coastal zone dinoflagellate Prorocentrum minimum was assumed to be the only constituent in a medium of clear ocean water. Pertinent optical parameters used in the simulations were the same as those used in Ref. 3 and are given in Table 1. The excitation source was assumed to be a laser with an emission wavelength of 480nm. Raman scattering at 574nm and fluorescence at 685nm were assumed to occur at sharp spectral lines; i.e., no effects of spectral bands for these events were considered. The scattering phase function for chlorophyll given in Fig. 2 that was used for this study is the same as that used by Poole and Esaias.[3] Ref. 3 gives appropriate discussions on the origins of the data in Table 1 and Fig. 2.

Results and Discussion

We have focused our study on the water Raman normalized Fluorescence signal, $R = H_F/H_R$, where H_F is the signal at 685nm received at the detector and H_R is the signal received at 574nm. In particular, we investigated R as a function of vertical concentration gradients for surface chlorophyll concentrations in the range from 0.01 to 20 μg/l. Simulation results for gradients of ± 20%, ± 15%, ± 10%, and ± 5% m^{-1} are shown in Fig. 3 where R is plotted as a function of surface concentration for each pair of gradients. The corresponding plot for a homogeneous medium with a concentration equal to the surface concentration of the analogue inhomogeneous media is shown on each graph for comparison. Error bars are within the size of the symbols used for plotting. The functional relation between R for a particular value of g, R_g, and surface concentration, C_o, for the data shown in Fig. 3 is of the form

$$R_g(C_o) = a\, C_o^{\,b} \quad , \tag{3}$$

where a and b are constants for a given gradient. It should be observed that since the values of b are near unity (ranging from 1.1 - 1.3), the data are well approximated by a linear relationship as indicated in Ref. 3. This is particularly the case when only the larger values of surface concentration are considered.

Absolute calibration of airborne fluorosensor measurements is practically impossible due to factors such as variation in phytoplankton fluorescence efficiency (or cross-section), both among the various species and also with environmental conditions (ambient light, nutrient levels, etc.). As a result, measurements are calibrated empirically by comparison with <u>in situ</u> sampling at or near the water surface; obviously, vertical inhomogeneities in chlorophyll concentration could lead to bias in the empirical calibration. To establish ranges of surface concentrations and/or vertical gradients in which calibration

by surface samples would be inappropriate, we have applied a one-tail t-test to determine at the 95% confidence level if R for a given vertical gradient is significantly different than the value of R computed for the analogous homogeneous medium. We assume that the results for the homogeneous and inhomogeneous cases represent independent samples. Approximately ten runs are made to obtain values for R for each gradient and for each surface concentration. The computer simulations are terminated when the variances in H_F and H_R fall below 5% of the values of H_F and H_R and at least 30 thousand photon packets have been sampled. We assume that our two sets of samples have common variances for the purpose of the t-test. Results of the t-test are given in Table 2. For media with high surface concentrations of chlorophyll ($\gtrsim$ 10 μg/l), the fluorosensor measurements are insensitive to vertical concentration gradients. For cases in which the surface concentrations are less than 1 μg/l, fluorosensor measurements were found to be sensitive to even the mildest gradients tested. For the intermediate range of surface concentrations (1 - 10 μg/l), the sensitivity of fluorosensor measurements to gradients was found to generally increase as the magnitude of the gradient increased. Significant differences (at the 95% confidence level) between the mean values of R for corresponding homogeneous and inhomogeneous cases occurred at surface concentrations of 1, 6, 6, and 10 μg/l for gradients of ± 5%, ± 10%, ± 15% and ± 20% m^{-1}, respectively.

Concluding Remarks

We have extended a semianalytic Monte Carlo radiative transfer simulation model for airborne laser fluorosensors to allow for inhomogeneities in the vertical distribution of consitutents in clear sea water. This article has presented results of the simulations for lineary varying step concentrations of chlorophyll. The results indicate that statistically significant

differences can be seen, under certain conditions, in the water Raman normalized fluorescence signals between nonhomogeneous and homogeneous cases. Generally, remote sensor users must exercise care when making empirical calibrations of airborne fluorosensors. The SALMON model has been used to show that fluorosensor measurements are sensitive to certain ranges of surface concentrations when the chlorophyll concentrations vary lineary with depth in the water medium.

References

1. L. R. Poole, D. D. Venable, and J. W. Campbell, Appl. Opt. 20, 3653 (1981).
2. L. R. Poole, Appl. Opt. 21, 3063 (1982).
3. L. R. Poole and W. E. Esaias, Appl. Opt. 21, 3756 (1982).
4. D. D. Venable, "A Radiative Transfer Model for Remote Sensing of Laser Induced Fluorescence of Phytoplankton in Nonhomogeneous Turbid Water," NASA CR 163155 (1980).
5. The distance, δ_k that a photon travels between events in homogeneous media without bounds is selected from a distribution function of the form $\delta_k = -\ln(\epsilon)/\alpha_T(\lambda)$, where ϵ is a random number uniformly distributed over the range $0 < \epsilon < 1$ and $\alpha_T(\lambda)$ is the total attenuation coefficient at wavelength λ for the medium. Adjustments are made to the distribution to account for interaction with the air-water interface.

Figure Captions

Figure 1 - Geometric arrangement of the fluorosensor system modeled by SALMON.

Figure 2 - Spectrally averaged scattering phase function for Prorocentrum minimum.

Figure 3 - Graphical representation of the Raman normalized fluorescence signal, $R = H_F/H_R$, vs surface concentration for gradients of (A) ± 20% m^{-1}, (B) ± 15% m^{-1}, (C) ± 10% m^{-1}, and (D) ± 5% m^{-1}. Δ - positive gradient, ∇ - negative gradient, and ◘ - homogeneous distribution.

List of Tables

Table 1: Optical Parameters

	Wavelength, nm		
	480 Excitation	574 Raman	685 Fluorescence
Absorption coefficient for P. minimum, $m^{-1}/(\mu g/liter)$	0.0582	0.0382	0.036
Scattering coefficient for P. minimum, $m^{-1}/(\mu g/liter)$	0.291	0.231	0.202
Fluorescence efficiency for P. minimum[a]	0.028	-	-
Absorption coefficient for clear ocean water, m^{-1}	0.0176	0.0911	0.475
Scattering coefficient for clear ocean water, m^{-1}	0.0034	0.0017	0.0007
Raman scattering coefficient, m^{-1}	0.0018	0.0009	0.0004

[a]Fluorescence at 685 nm considered only for excitation photons at λ = 480 nm.

Table 2: Confidence Limits for Detecting Significant Differences Between Mean Values of R for Corresponding Homogeneous and Inhomogeneous Cases

Surface Concentration µg/l	Gradient ± 20% m^{-1}	Gradient ± 15% m^{-1}	Gradient ± 10% m^{-1}	Gradient ± 5% m^{-1}
0.01	99+	99+	99+	99+
0.03	99+	99+	99+	99+
0.1	99+	99+	99+	99+
0.3	99+	99+	99+	99+
1	99+	99+	99+	98
3	99+	99+	96	89
6	98	99	95	90
10	95	92	88	54
15	86	51	78	58
20	79	77	67	58

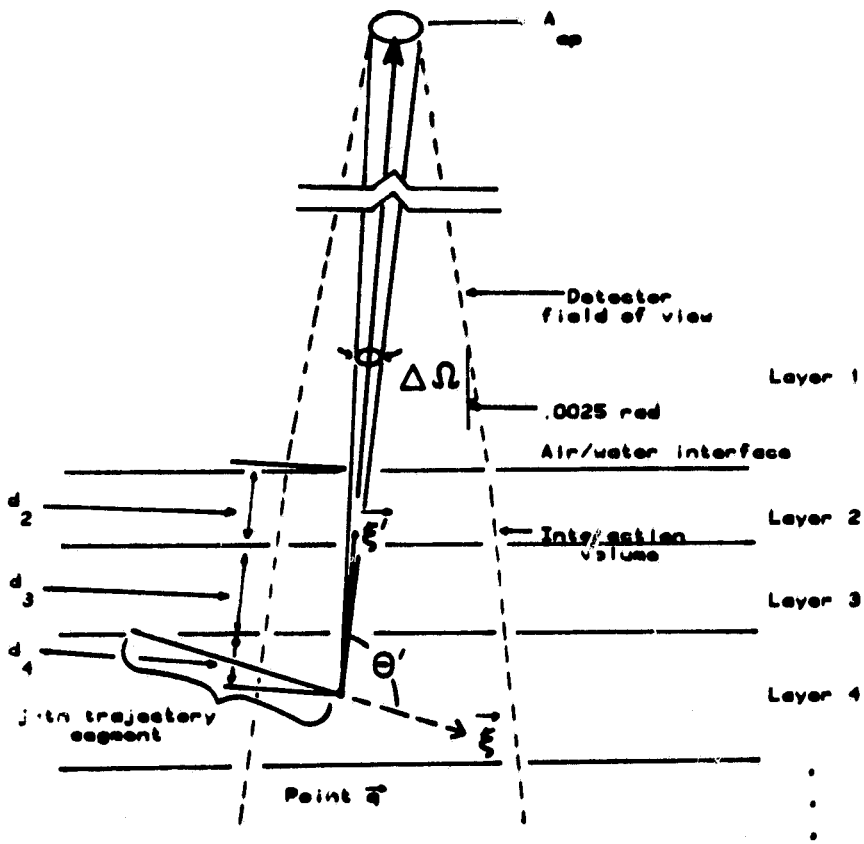

Figure 1

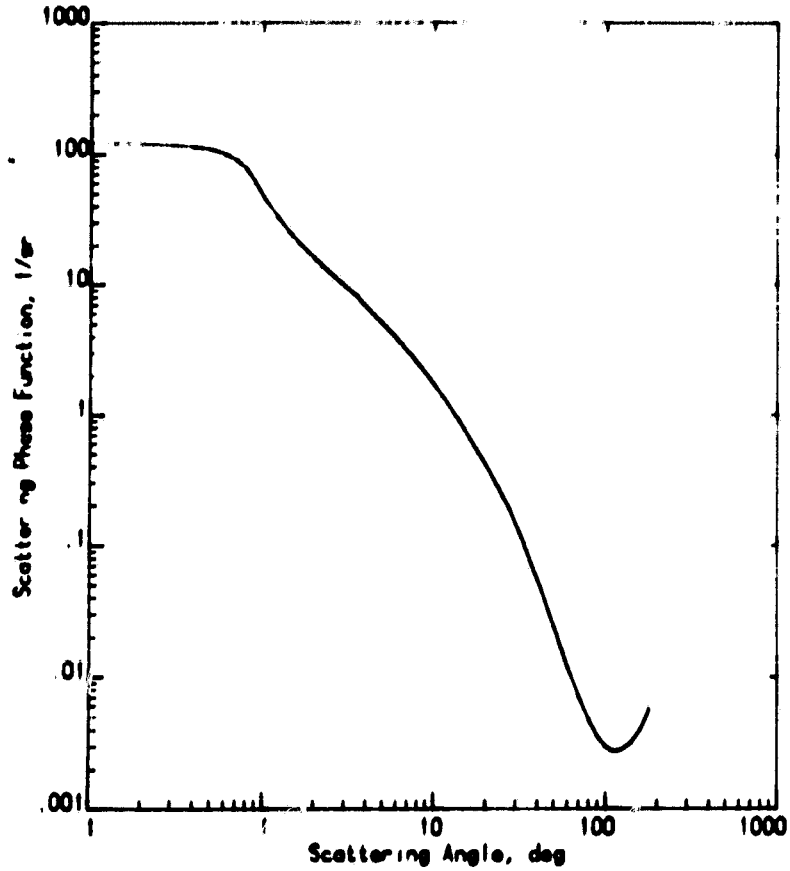

Figure 2

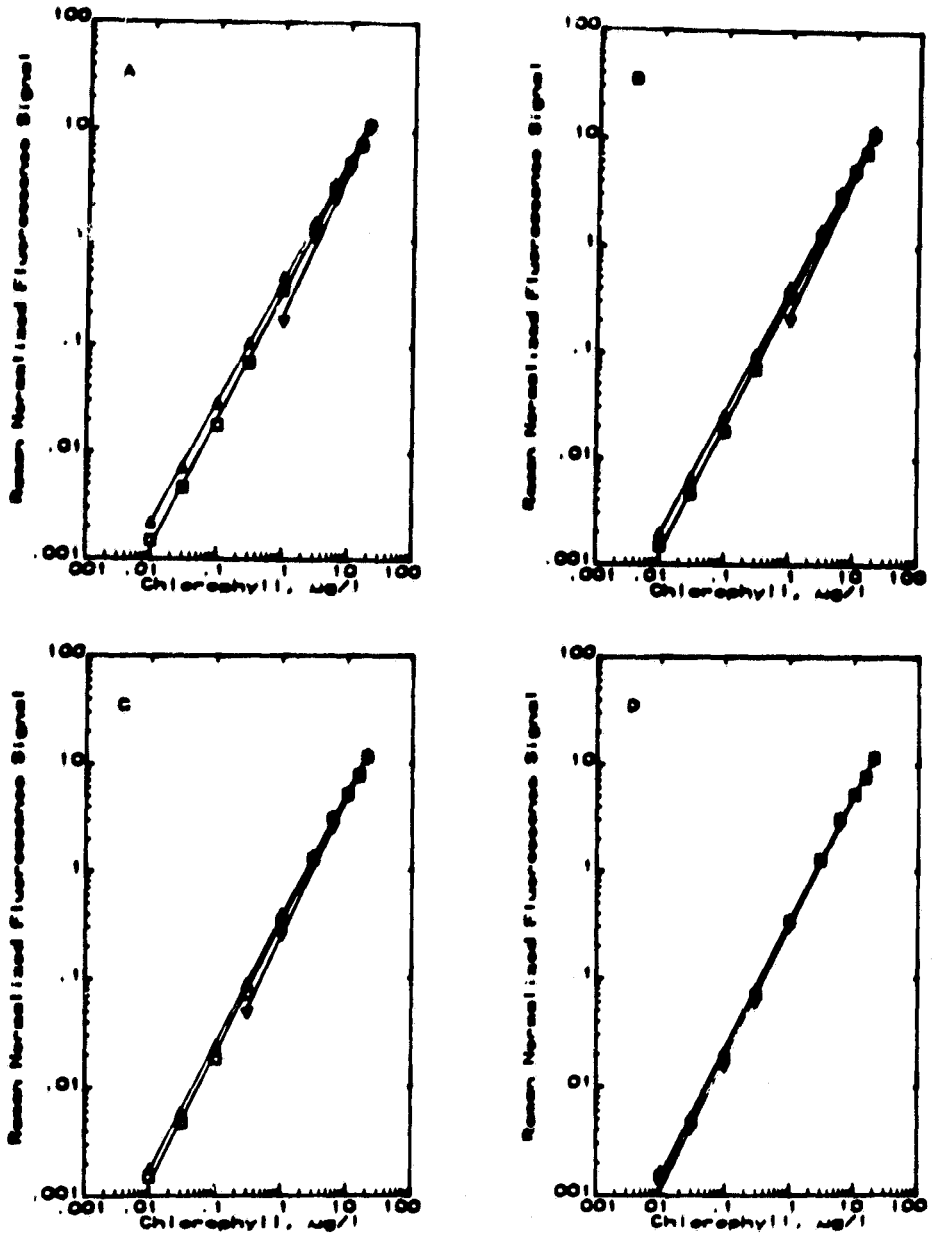

Figure 3

Chapter 3

SALMON Modifications for Non-homogeneous Media

A. R. Punjabi

Introduction

We have employed the semianalytic Monte Carlo radiative transfer model (SALMON)[1] to investigate the effects of inhomogeneities in the phytoplankton concentrations in the clear sea waters on the lidar signals. In this model, the detector signal is evaluated through a combination of stochastic and analytic techniques. This makes it possible to model lidar systems with realistic geometric constraints such as small, finite detector fields of view. Inclusion of analytic estimates for various stochastic processes reduces the computer resources required to use the model. Convergence in the SALMON model is virtually independent of collector size. Significant statistical advantages are gained by splitting true Raman photons and modifying virtual interactions.[2-4]

The geometry of the physical set up used in our investigation is shown in Fig. 1. A_{ap} is the area of detector aperture (0.071 cm^2). Layer 1 is air. Broken lines in the layer 1 represent the detector field of view (0.0025 radians). However, the SALMON simulation code can handle 1 to 5 fields of view. The detector is located at a height of 150 m above the top of water surface which is perfectly flat. The clear water medium containing phytoplankton is divided into layer 2 through layer 21. Concentration of chlorophyll is constant in each layer but varies linearly from layer to layer as one advances from top of layer 2 downwards. For a given surface concentration layers 2 to 20 have equal thicknesses. The bottom of layer 21 is 999 ms below the air-water interface for all values of surface concentration. The thickness of 21st layer is set to such a large value to ensure that the photons do not reach the bottom of medium. Thicknesses of layers 2 to 20 is large (small) for small (large) surface concentrations. Each layer is completely homogeneous in the chlorophyll concentration. No lateral variations are allowed in chlorophyll concentration. The linearly varying profile of chlorophyll concentration in water medium is approximated by a step function profile.

In Fig. 1, $\vec{q}$ is the terminal point of j^{th} trajectory of the photon packet, $\vec{q}$ is its direction of travel. θ' is the angle through which the photon at point $\vec{q}$ must be scattered in order to be collected by the detector within the solid angle $\Delta\Omega$. Broken lines in layers 2 to 21 define the boundaries of the interaction volume.[1]

Fig. 2 is the flow chart for the SALMON simulation code. The number of events N_e per sample is limited to 1000, and number of samples is restricted to a maximum of 120 with a minimum size of 30 samples.

Input Parameters and Other Pertinent Quantities

Optical parameters used in our computations are shown in Table 1. In this study, the common coastal zone dinoflagellate Prorocentrum minimum is assumed to be the only constituant in a medium of clear sea water. Pertinent optical parameters used in the simulation are the same as those used in Ref. 2. The spectrally averaged volume scattering phase function for Prorocentrum minimum, which we have used in this study, is the one used by Poole and Esaias[2], and is shown is Fig. 3. Ref. 2 gives appropriate discussions on the origin of data in Table 1 and Fig. 3.

The surface concentration of chlorophyll is denoted by C_o. The concentration for the medium is denoted by $C(z)$, where z is the depth in the medium. The downward direction taken as positive. The gradient in chlorophyll concentration, denoted by g, is defined to be

$$g = \frac{1}{C_o} \frac{dC(z)}{dz} \qquad (1)$$

and is given in units of m^{-1}. In the stratified model, the concentration assigned to k^{th} layer is the averaged value of $C(z)$ at the top and bottom of the layer. Concentration in the 21st layer is assigned so that the difference in concentrations for the 21st and 20th layer is the same as the difference in concentrations for the 20th and 19th layers.

Z_{90} is defined as the depth from which 90% of detector signal at a particular wavelength emanates for a homogeneous concentration corresponding to C_o. $Z_{90,max}$ is defined as the maximum of the Z_{90} for laser wavelength ($Z_{90,\ \lambda_L}$), Z_{90} for the Raman wavelength ($Z_{90,\ \lambda_R}$) and Z_{90} for the fluorescent wavelength ($Z_{90,\ \lambda_F}$), i.e.

$$Z_{90,max}\ (\lambda_L,\ C_o) = \max \{ Z_{90,\ \lambda_L}\ (C_o),\ Z_{90,\ \lambda_R}\ (C_o),\ Z_{90,\ \lambda_F}\ (C_o) \} \qquad (2)$$

Note that $Z_{90,max}$ depends on the laser excitation wavelength λ_L and the value of surface concentration C_o. Z_{90}'s used in equ. (2) are for the homogeneous medium and are taken from Ref. 2. Fig. 4 shows Z_{90} vs. C_o for λ_L=532 and 480 nm. The excitation source is assumed to be a laser with emission wavelength of 480 nm or 532 nm. Raman scattering at 574 nm and fluorescence at 685 nm are assumed to occur at sharp spectral lines; no effects of spectral bands for these events are considered.

For a given surface concentration, the depth z_o in the water medium below which the concentration C(z) vanishes for negative gradients g, depends upon g and C_o. Z_o is defined as

$$C(z \geq z_o) \leq 0\ ,\ g < 0\ . \qquad (3)$$

z_o may be smaller than $Z_{90,max}$ for a given excitation wavelength when g is a sufficiently large negative number. Table 2 shows Δz and $Z_{90,max}$ for various values of surface concentrations C_o where Δz is the thickness of layers 2 through 20. Table 2 is for excitation wavelength λ_L=480 nm. This table also indicates the depth z_o for values of gradients g = -20% m^{-1}, -15% m^{-1}, 10% m^{-1} and -5% m^{-1}. Solid demarcating line in the last 4 columns of this table separate the C_o regime for which $z_o < Z_{90,max}$ from the C_o regime for which $z_o > Z_{90,max}$. For example, for a gradient of -20% m^{-1} and surface concentration below 1.0 μg/l, z_o is smaller than $Z_{90,max}$. C* denotes the value of C_o for which z_o is smaller than $Z_{90,max}$ for a given gradient for all $C_o \leq C^*$. Table 3 shows C* for various values of gradients for λ_L=480 nm.

In this study, we have considered the range of surface concentrations from 0.01 μg/l to 20 μg/l, while the range of gradients is -20% m^{-1} to 20% m^{-1}. Table 3 is based on these ranges of values of C_o and g. It must be pointed out that for excitation wavelength λ_L=532 nm, $|Z_{90,max}|$ is always smaller than $|z_o|$ for the ranges of C_o and g considered in our study. This distinction between the two excitation wavelengths λ_L=480 nm and 532 nm is of considerable significance in this study. For λ_L=480 nm, we can see from Fig. 4 that $Z_{90,\ \lambda_R}$ is large compared to $Z_{90,\ \lambda_F}$ or $Z_{90,\ \lambda_L}$ for small values of surface concentration. Thus, $Z_{90,max} = Z_{90,\ \lambda_R}$ for λ_L=480 nm. Thus, in this case, when surface concentrations are equal to or less than C*, the detector receives 90% or more of signal at fluorescent wavelength while less than 90% of signal is received at Raman wavelength. This asymmetry between signals received at the Raman and fluorescent wavelengths becomes manifested when we examine the Raman normalized fluorescence signals as function of surface concentration for a given gradient when $C_o > C^*$. We will observe that such points of asymmetry do not give good fits to the simulation results. While we will also observe that no such difficulty arises for excitation wavelength λ_L=532 nm.

In the following discussion, we denote the detector signal received at the Raman wavelength by H_R, while the detector signal received at the fluorescence wavelength is denoted by H_F. Both H_F and H_R are functions of the excitation wavelength λ_L, the gradient in chlorophyll concentration g and the surface concentration C_o. The Raman normalized fluorescence signal is denoted by R, where

$$R(\lambda_L,\ C_o,\ g) = H_F(\lambda_L,\ C_o,\ g)/H_R(\lambda_L,\ C_o,\ g) \qquad (4)$$

For a fixed surface concentration C_o and gradient g, ten computer runs are made. Outcome of a particular run is accepted if 95% of the samples have 10% or less deviation in signals H_F and H_R. R is then calculated for each successful computer run from eqn. (4) and the standard deviation in R, σ_R is calculated

from the relation

$$\sigma_R = R\ \{(\sigma^2_{H_F}/H^2_F) + (\sigma^2_{H_R}/H^2_R)\}^{\frac{1}{2}} \qquad (5)$$

where σ_{H_F} and σ_{H_R} are standard deviations in H_F and H_R respectively. Then the mean values of R and standard deviation σ_R are the weighted averages of P and σ_R, given by

$$\langle R \rangle = \frac{\sum_{i=i}^{n} (R_i / {}^{2}R_i)}{\sum_{i=i}^{n} (1/ R_i^2} \qquad (6)$$

and

$$\langle \sigma_R \rangle = \pm \{1/ \sum_{i=i}^{n} (1/\sigma^2_{R_i})\}^{\frac{1}{2}} \qquad (7)$$

where

$$n \leq 10$$

For the remainder of this report, R will represent $\langle R \rangle$ and σ_R will represent $\langle \sigma_R \rangle$.

Results and Discussion

Tables 4 and 5 show R and σ_R values as functions of surface concentration C_o and gradient g for excitation wavelengths λ_L=480nm and 532nm respectively.

Let us first consider the simulation results for λ_L=480nm. We first attempted to fit the simulation results of R vs C_o, for a given g, by a straight line with zero intercept. However, this fit was quite poor for low surface concentrations. The reason for requiring a zero intercept is that when chlorophyll concentration vanishes, the fluorescence signal H_F will vanish. A straight line with zero intercept can be represented by

$$R(C_o, g) = m(g)\ C_o \tag{8}$$

where m is the slope and m varies with gradient. $\sigma_m(g)$ is the standard deviation in m. It must be mentioned that for λ_L=480nm, we fit only those points for which $z_o > Z_{90,max}$. If we attempt to fit all points (including those for which $z_o < Z_{90,max}$), the overall quality of fit deteriorates. When we plot log R vs log C_o for a given gradient g, a straight line gives a good fit. Figs. 5(a) - (d) show this power law fit for λ_L=480nm. The power law relation is

$$R(C_o, g) = A\ C_o^B \tag{9}$$

where the scaling factor A and the exponent B are functions of g alone for a given λ_L. σ_A and σ_B represent standard deviations in A and B respectively and are functions of g.

Figs. 6(a) - (d) show straight line fits (with zero intercept) for the λ_L=532nm simulation results. Figs. 7(a) - (d) show power law fits for the same excitation wavelength. It is clear that a straight line fit with zero intercept is more satisfactory in case of green laser than in case of blue laser. However, in both cases, the power law fit is superior to the straight line fit.

Tables 6(a) and (b) show the fitting parameters m, A & B and standard deviations σ_A and σ_B as functions of gradient for λ_L=480 and 532nm respectively. Note that both A and m decrease with gradient while B increases as the gradient decreases for both excitation wavelengths. Uncertainties σ_A and σ_B for both excitation wavelengths become larger as the gradient becomes smaller for positive values through negative values. Fitting parameter B for the λ_L=532nm case is very close to unity for all values of g. Also, m and A are quite comparable for λ_L=532nm. The standard deviations, σ_A and σ_B, for λ_L=532nm are smaller than those for λ_L=480nm for all values of g.

Now we define two goodness-of-fit parameters, X_1^2 and X_2^2, as

$$X_1^2 = \frac{1}{N} \sum_{i=i}^{N} (R_{fit} - R_i)/R_i \quad ^2 \tag{10}$$

and

$$X_2^2 = \frac{1}{N} \sum_{i=i}^{N} (R_{fit} - R_i)^2 \tag{11}$$

where R_{fit} is given by eqn. (8) for a straight line fit with zero intercept and by eqn. (9) for a power law fit. X_1^2 weighs each R_i equally. In eqns. (10) and (11) above, N is the number of points. Thus X_1^2 weighs R for small and large concentrations equally. While X_2^2 weighs R for large C_o heavily compared to R for small C_o, for a given g. We also define P_2 as ratio of X_2^2 for straight line fit to X_2^2 for power law fit, and P_1 as the ratio of X_1^2 for straight line fit to X_1^2 for power law fit, i.e.

$$P_2 = \frac{X_2^2, \text{ straight line fit}}{X_2^2, \text{ power law fit}} \tag{12}$$

and

$$P_1 = \frac{X_1^2,\ \text{straight line fit}}{X_1^2,\ \text{power law fit}} \tag{13}$$

Tables 7(a) and (b) give X_1^2, X_2^2, P_1 and P_2 for both straight line fit and power law fit for λ_L=480 and 532nm, respectively.

From Tables 7(a) and (b) we see that, for high surface concentrations, a straight line fit is as good as a power law fit and it is all the more so in the case of the green laser. While if we consider all surface concentrations, a power law fit is definitely far superior to a straight line fit for both blue and green lasers. Thus we can definitely conclude that a power law relationship given by eqn. (9) is the better analytic representation of the computational results.

Let us examine the average values of X_1^2 and X_2^2 for both straight line fits and power law fits for λ_L=480 and 532nm as

$$\begin{aligned} \langle X_1^2 \rangle &= \frac{1}{9} \sum_g X_{1,g}^2 \\ \langle X_2^2 \rangle &= \frac{1}{9} \sum_g X_{2,g}^2 \end{aligned} \tag{14}$$

where the summation is over various values of gradient g. Table 8 shows these average values. This table clearly shows that a power law fit is better and that computational results for green laser fit better.

If we fix the surface concentration C_o and average σ_R over all values of gradient g, we get an average value for σ_R, denoted by $\langle \sigma_R \rangle_g$, as a function of C_o. This can be expressed as

$$\langle \sigma_R \rangle_g = \frac{1}{9} \sum_g \sigma_{R,g} \tag{15}$$

where again the summation is over various values of gradient g. Table 9 lists $\langle \sigma_R \rangle_g$ for both excitation wavelengths. We observe from this table that errors in R, the Raman normalized fluorescence signal, are smaller at low values of surface

concentration and also that for C_o=0.01 to 3 μg/l, $\langle\sigma_R\rangle_g$ are smaller for green laser than for blue laser and for C_o > 3 μg/l, the opposite is true.

In Figs. 8(a) and (b) we show power law curves and computational points for gradients g = 20% m^{-1}, 0% m^{-1} and -20% m^{-1} for blue and green lasers respectively. Figs. 9(a) and (b) show power law fitting parameters A and B vs gradient g for blue and green lasers respectively.

Fig. 9 and Tables 4 and 5 show that signal ratio R is higher (lower) for positive (negative) gradients as compared to the homogeneous case for all values of surface concentrations considered in this study. The exponent in the power law fitting function decreases as gradient g increases from -20% m^{-1} through 0% m^{-1} to -20% m^{-1}.

The upper limits on the range of surface concentration values beyond which error bars on $R(C_o, g)$ and $R(C_o, g=o)$ and/or $R(C_o, g=o)$ and $R(C_o, -g)$ overlap are denoted by C_{oL} and are shown in Table 10. This table shows that blue and green laser results are similar so far as overlapping of signals from homogeneous media with the one from inhomogeneous media is concerned. As is expected, the upper bound on the range of surface concentrations within which signals do not overlap reduces with decreasing magnitude of gradient.

We have also performed one tailed T tests with unequal variances to determine distinguishability of $R(C_o, \pm g)$ from $R(C_o, g=0)$. Tables 11(a) and (b) show the results of these tests. The tables show the probabilities α_+ or α_- that signal $R(C_o, \pm g)$ is greater (or less) than $R(C_o, g=o)$. α is the smaller of α_+ and α_- for a given C_o. We see that for lower surface concentrations, signal R for a given positive or negative gradient is distinctly higher or lower than R for zero gradient. Thus, for smaller surface concentrations, R from inhomogeneous media can easily be distinguished from the R from a homogeneous media with the same surface concentration C_o.

We define C_{Res} as the upper limit on C_o beyond which sigral R from an inhomogeneous media with a given magnitude of gradient, $|g|$, can not be distinguished from R from a media with g=o, with $\alpha > 95\%$. Table 12 lists C_{Res} as a function of $|g|$.

From Tables 11 and 12, we see that the range of surface concentrations for which signals can be resolved between homogeneous and inhomogeneous media becomes smaller as the magnitude of gradient becomes smaller, as can be expected. C_{Res} for green laser are better than C_{Res} for blue laser. Thus green laser will resolve signals (between homogeneous and inhomogeneous media) better, i.e. for wider range of surface concentrations.

Conclusions

We have employed the semianalytic Monte Carlo simulation methodology towards the following ends:

(i) To determine how the lidar signals from an inhomogeneous media differ from ones from homogeneous media.

(ii) To determine an analytic representation of simulation results.

(iii) To compare the performance of blue and green lasers.

In the SALMON simulations we performed, the linearly varying vertical chlorophyll concentration profiles have been approximated by step function profiles. For this reason, we refer to the simulation model as the stratified SALMON model. The two parameters which we use to specify the inhomogeneous media are C_o, the surface concentration and g, the gradient in concentration.

The simulations have shown that the Raman normalized fluorescence signal, R, is generally higher (lower) for higher (lower) surface concentrations C_o and gradients g. R is high for positive gradients compared to zero gradient. Opposite results are true for negative gradients in chlorophyll concentrations. It is easier to dintinguish media having different gradients at lower values of surface concentrations. At high values of surface concentrations, the differences in the signals from media having different gradients overlap and can not be distinguished. The range of surface concentrations and the upper bound of this range for which signals from media having a fixed non-zero magnitude of gradient can be differentiated from those which emanate from homogeneous media reduces as the gradient becomes smaller. In short, lower concentrations and high gradients yield better resolution and distinguishability of signals.

The normalized signal R and the surface concentration C_o can be approximated by an analytic expression of the form

$$R\ (C_o,\ g) = A\ (g)\ C_o^{B(g)} \qquad (16)$$

In this power law relationship, the scaling factor A and the exponent B are functions of g alone and both show a definite trend in their relationship to g (see Fig. 9). This power law fit is better for small C_o's as compared to high C_o's. Since error bars on A and B do not overlap beyond more than 10% m^{-1} difference in gradients, this analytic representation is good for media having gradients differing by more than 10% m^{-1}.

The relative error in R given by σ_R/R, where σ_R is the standard deviation in R, are smaller for green laser excitation than those for blue laser excitation. Power law fits for λ_L=532nm are superior to those for λ_L=480nm. Green laser excitation can resolve greater range of surface concentrations than blue laser excitation. Thus the computational results show that results for green laser are more satisfactorily standarizable (by an analytic expression) and more widely applicable (for the purpose of distinguishability of signals) than those for blue laser.

References

1. L. R. Poole, D. D. Venable and J. W. Campbell, Applied Optics, 20, 3653 (1981).
2. L. R. Poole and W. E. Esaias, Applied Optics, 21, 3756 (1982).
3. L. R. Poole, Applied Optics, 22, 380 (1983).
4. R. J. Exton, W. M. Houghton, W. E. Esaias, R. C. Harris, F. H. Farmer, NOAA, National Ocean Survey, private communication.

List of Tables

TABLE 1: Optical Parameters

	Wavelength , nm		
	480 Excitation	574 Raman	685 Fluorescence
Absorption coefficient for P. minimum, /m/(µg/l)	0.0582	0.0382	0.036
Scattering coefficient for P. minimum, /m/(µg/l)	0.291	0.231	0.202
Fluorescence efficiency for P. minimum [a]	0.028	-	-
Absorption coefficient for clear ocean water,/m	0.0176	0.0911	0.475
Scattering coefficient for clear ocean water , /m	0.0034	0.0017	0.0007
Raman scattering coefficient,/m	0.0018	0.0009	0.0004

[a] Fluorescence at 685 nm considered only for excitation wavelength at 480 nm.

TABLE 2

EXCITATION WAVELENGTH=480 nm.

C_0 (µg/l)	Δ (m)	$Z_{90,max}$ (m)	d_0 (m) g (/m) -20%	-15%	-10%	-5%
.01	2.0	18.0	6.0	8.0	12.0	22.0
.03	2.0	17.0	6.0	8.0	12.0	22.0
.1	2.0	13.5	6.0	8.0	12.0	22.0
.3	2.0	9.0	6.0	8.0	11.0	22.0
1.	1.0	5.0	6.0	8.0	11.0	
3.	1.0	3.0				
6.0	0.1	2.0				
10.0	0.1	1.8				
15.0	0.1	1.6				
20.0	0.1	1.4				

TABLE 3

EXCITATION WAVELENGTH=480 nm.

C^* (µg/l)	α (/m)
0.3	-20%
0.1	-10%

TABLE 4

CONC (µg/l)	R 20	S 20	R -20	S -20	R 15	S 15	R -15	S -15
20.	12.0500	0.38000	10.6000	0.32470	12.3688	0.40790	10.5160	0.33500
15.	8.4700	0.21500	7.3200	0.20590	8.0850	0.23860	7.6222	0.19890
10.	5.5700	0.13400	4.5570	0.12270	5.4190	0.11710	4.6800	0.12610
6.	3.3500	0.08000	2.3990	0.06930	3.3070	0.07520	2.5200	0.06840
3.	1.4800	0.04230	1.0309	0.02890	1.4490	0.03640	1.1100	0.02280
1.	0.4520	0.00670	0.1708	0.00220	0.4162	0.00610	0.2038	0.00280
0.3	0.1080	0.00110	0.0337	0.00020	0.0993	0.00095	0.0398	0.00030
0.1	0.0290	0.00016	0.0093	0.00006	0.0262	0.00018	0.0107	0.00007
0.03	0.0072	0.00004	0.0027	0.00002	0.0066	0.00003	0.0031	0.00002
0.01	0.0022	0.00001	0.0009	0.00001	0.0020	0.00001	0.0010	0.00001

CONC (µg/l)	R 10	S 10	R -10	S -10	R 5	S 5	R -5	S -5
20.	12.1200	0.41890	10.9000	0.38800	11.9040	0.41480	10.9980	0.44810
15.	8.1200	0.21900	7.8700	0.20580	7.6981	0.21650	7.7830	0.19590
10.	5.3800	0.11800	4.9400	0.11700	5.3114	0.11580	5.0700	0.12100
6.	3.2500	0.07250	2.5700	0.06810	3.1862	0.06980	2.7200	0.06380
3.	1.3900	0.03630	1.1590	0.02630	1.3073	0.02550	1.2300	0.02600
1.	0.3960	0.00610	0.2510	0.00350	0.3565	0.00680	0.2993	0.00430
0.3	0.0897	0.00074	0.0470	0.00040	0.0804	0.00070	0.0595	0.00600
0.1	0.0236	0.00015	0.0120	0.00008	0.0211	0.00013	0.0151	0.00009
0.03	0.0059	0.00003	0.0035	0.00002	0.0053	0.00003	0.0041	0.00002
0.01	0.0018	0.00001	0.0011	0.00001	0.0017	0.00001	0.0013	0.00001

CONC (µg/l)	R 0	S 0
20.	11.4990	0.34790
15.	7.6066	0.21380
10.	5.1698	0.11390
6.	3.0520	0.07350
3.	1.2700	0.02620
1.	0.3386	0.00560
0.3	0.0708	0.00070
0.1	0.0182	0.00010
0.03	0.0047	0.00003
0.01	0.0015	0.00001

TABLE 5

CONC (µg/l)	R 20	S 20	R -20	S -20	R 15	S 15	R -15	S -15
20.	13.1634	0.45550	12.0213	0.48290	13.1155	0.53610	12.0645	0.48690
15.	9.6006	0.28510	8.8517	0.31110	9.2735	0.27810	9.0512	0.27210
10.	7.0923	0.18020	5.3332	0.16170	6.9307	0.17340	5.5008	0.14420
6.	4.0687	0.10250	3.0572	0.07940	3.9014	0.08040	3.1633	0.09270
3.	1.9477	0.03860	1.3757	0.03010	1.9432	0.03880	1.4992	0.03080
1.	0.6793	0.00802	0.3715	0.00468	0.6388	0.00920	0.4110	0.00530
0.3	0.2026	0.00196	0.0995	0.00063	0.1909	0.00170	0.1113	0.00072
0.1	0.0665	0.00039	0.0305	0.00015	0.0634	0.00032	0.0346	0.00018
0.03	0.0205	0.00008	0.0090	0.00005	0.0190	0.00008	0.0103	0.00005
0.01	0.0068	0.00003	0.0030	0.00002	0.0063	0.00003	0.0034	0.00002

CONC (µg/l)	R 10	S 10	R -10	S -10	R 5	S 5	R -5	S -5
20.	12.6517	0.51960	11.9938	0.52122	12.7848	0.39510	12.1511	0.50700
15.	9.4307	0.27670	9.1788	0.29170	8.9728	0.26710	9.4645	0.31180
10.	6.7239	0.19840	5.7455	0.16910	6.5347	0.18230	5.7460	0.15880
6.	3.9547	0.09870	3.3352	0.10800	3.7819	0.10260	3.4387	0.10150
3.	1.9056	0.03730	1.5305	0.04010	1.8361	0.04060	1.5671	0.04110
1.	0.6070	0.00780	0.4553	0.00530	0.5671	0.00770	0.4940	0.00590
0.3	0.1786	0.00140	0.1239	0.00089	0.1642	0.00130	0.1381	0.00094
0.1	0.0592	0.00032	0.0393	0.00023	0.0543	0.00027	0.0444	0.00022
0.03	0.0175	0.00007	0.0117	0.00005	0.0161	0.00007	0.0131	0.00006
0.01	0.0058	0.00002	0.0039	0.00002	0.0053	0.00002	0.0043	0.00002

CONC (µg/l)	R 0	S 0
20.	12.3891	0.38440
15.	8.9357	0.27510
10.	6.1025	0.15220
6.	3.5820	0.08670
3.	1.8310	0.05070
1.	0.5347	0.00690
0.3	0.1509	0.00110
0.1	0.0492	0.00023
0.03	0.0146	0.00007
0.01	0.0048	0.00002

TABLE 6(a)

EXCITATION WAVELENGTH=480 nm.

g (/m)	m	A	B	S_A	S_B
+20%	0.5635	0.4131	1.1384	0.0068	0.0064
+15%	0.5624	0.3921	1.1514	0.0073	0.0069
+10%	0.5554	0.3721	1.1663	0.0072	0.0075
+5%	0.5387	0.3468	1.1797	0.0079	0.0089
0%	0.5264	0.3235	1.1962	0.0089	0.0107
-5%	0.5083	0.2948	1.2154	0.0102	0.0134
-10%	0.5017	0.2447	1.2958	0.0109	0.0225
-15%	0.4847	0.2296	1.3030	0.0208	0.0434
-20%	0.4742	0.1959	1.3751	0.0203	0.0498

TABLE 6(b)

ρ	m	A	B	S_A	S_B
(/m)					
+20%	0.6648	0.6733	0.9962	0.0062	0.0036
+15%	0.6509	0.6443	1.0048	0.0059	0.0036
+10%	0.6410	0.6189	1.0161	0.0053	0.0033
+5%	0.6261	0.5855	1.0264	0.0063	0.0047
0%	0.6060	0.5521	1.0370	0.0062	0.0044
-5%	0.5972	0.5158	1.0508	0.0075	0.0057
-10%	0.5847	0.4834	1.0673	0.0082	0.0067
-15%	0.5744	0.4507	1.0847	0.0101	0.0087
-20%	0.5619	0.4173	1.1018	0.0112	0.0105

TABLE 7(a)

EXCITATION WAVELENGTH=480 nm.

g	St. line fit		Power law fit		P_1	P_2
(/m)	$(\alpha_1)^2$	$(\alpha_2)^2$	$(\alpha_1)^2$	$(\alpha_2)^2$		
+20%	0.5531	0.0892	0.0021	0.0546	1.2	257.4
+15%	0.7602	0.1510	0.0026	0.0678	2.2	291.7
+10%	1.0160	0.1209	0.0030	0.0487	2.5	342.7
+5 %	1.3070	0.1568	0.0041	0.0691	2.3	321.6
0%	1.7730	0.1187	0.0061	0.0540	2.2	292.6
-5%	2.4580	0.0967	0.0097	0.0158	6.1	252.4
-10%	0.8512	0.1822	0.0050	0.1511	1.2	169.3
-15%	0.3378	0.1956	0.0080	0.1401	1.4	43.9
-20%	0.5580	0.2966	0.0101	0.1439	2.0	55.5

TABLE 7(b)

EXCITATION WAVELENGTH=532 nm.

g	St. line fit		Power law fit		P_1	P_2
(/m)	$(\alpha_1)^2$	$(\alpha_2)^2$	$(\alpha_1)^2$	$(\alpha_2)^2$		
+20%	0.0009	0.0355	0.0007	0.0354	1.0	1.4
+15%	0.0010	0.0428	0.0007	0.0443	1.0	1.4
+10%	0.0039	0.0174	0.0008	0.0294	0.6	6.8
+5%	0.0119	0.0328	0.0009	0.0333	1.0	12.6
0%	0.0237	0.0107	0.0010	0.0072	1.5	23.0
-5%	0.0550	0.0422	0.0017	0.0381	1.1	32.7
-10%	0.1035	0.0307	0.0024	0.0272	1.3	43.7
-15%	0.1860	0.0742	0.0040	0.0503	1.5	46.3
-20%	0.3065	0.1111	0.0060	0.0857	1.3	51.5

TABLE 8

Excitation wavelength (nm)	St. line fit (χ_1^2)	St. line fit (χ_2^2)	Power law fit (χ_1^2)	Power law fit (χ_2^2)
480	1.0683	0.1584	0.0056	0.0833
532	0.0769	0.0448	0.0020	0.0390

TABLE 9

Surface Concentration	Average Error $\langle S_{R_f} \rangle$	
	Excitation Wavelength	
C_0 (µg/l)	480 nm	532 nm
0.01	0.0118	0.0096
0.03	0.0116	0.0092
0.1	0.0125	0.0104
0.3	0.0177	0.0152
1.0	0.0300	0.0254
3.0	0.0472	0.0453
6.0	0.0507	0.0531
10.0	0.0473	0.0548
15.0	0.0541	0.0621
20.0	0.0673	0.0765

TABLE 10

Ig(l/m)	C_{OL} (µg/l) Excitation wavelength	
	480 nm	532 nm
20%	10.0	10.0
15%	10.0	10.0
10%	6.0	1.0
5%	1.0	1.0

TABLE 11(a)

C_0 (µg/l)	Gradient (/m)											
	20%	-20%		15%	-15%		10%	-10%		5%	-5%	
	α_+	α_-	α	α_+	α_-	α	α_+	α_-	α	α_+	α_-	α
00.01	>99	>99	>99	>99	>99	>99	>99	>99	>99	>99	>99	>99
00.03	>99	>99	>99	>99	>99	>99	>99	>99	>99	>99	>99	>99
00.1	>99	>99	>99	>99	>99	>99	>99	>99	>99	>99	>99	>99
00.3	>99	>99	>99	>99	>99	>99	>99	>99	>99	>99	>99	>99
1.0	>99	>99	>99	>99	>99	>99	>99	>99	>99	98	>99	98
3.0	99	>99	99	>99	>99	>99	96	>99	96	89	90	89
6.0	98	>99	98	99	>99	99	95	>99	95	90	>99	90
10.0	95	96	95	92	99	92	90	86	86	81	54	54
15.0	96	86	86	87	51	51	80	78	78	58	66	58
20.0	79	88	79	77	89	77	67	82	67	58	66	58

TABLE 11(b)

C_0 (μg/l)	Gradient (/m)											
	20%	-20%		15%	-15%		10%	-10%		5%	-5%	
	α_+	α_-	α	α_+	α_-	α	α_+	α_-	α	α_+	α_-	α
00.01	>99	>99	>99	>99	>99	>99	>99	>99	>99	>99	>99	>99
00.03	>99	>99	>99	>99	>99	>99	>99	>99	>99	>99	>99	>99
00.1	>99	>99	>99	>99	>99	>99	>99	>99	>99	>99	>99	>99
00.3	>99	>99	>99	>99	>99	>99	>99	>99	>99	>99	>99	>99
1.0	>99	>99	>99	>99	>99	>99	>99	>99	>99	99	>99	99
3.0	98	>99	98	98	>99	98	96	93	>99	89	90	89
6.0	>99	>99	>99	98	>99	98	96	90	90	88	71	71
10.0	98	>99	98	99	>99	99	98	98	98	92	98	92
15.0	92	65	65	79	68	68	85	79	79	53	88	53
20.0	81	79	79	77	80	77	68	82	68	69	76	69

TABLE 12

Ig (/m)	C Res (µg/l) Laser Wavelength 480 nm	532 nm
20%	10.0	10.0
15%	6.0	10.0
10%	6.0	10.0
5%	1.0	1.0

Figure Captions

1. Geometry of the physical set up used in our investigation.
2. Flow chart for SALMON simulation code.
3. Spectrally averaged volume scattering phase function for Prorocentrum minimum.
4. Z_{90} vs. C_o for λ_L=480 and 532 nm.
5. Power-law fits for λ_L=480 nm.
   (a) g = 20% m^{-1}, 0% m^{-1} and -20% m^{-1},
   (b) g = 15% m^{-1}, 0% m^{-1} and -15% m^{-1},
   (c) g = 10% m^{-1}, 0% m^{-1} and -10% m^{-1},
   (d) g = 5% m^{-1}, 0% m^{-1} and -5% m^{-1}.
6. Straight line (with zero interapt) fits for λ_L=532 nm.
   (a) g = 20% m^{-1}, 0% m^{-1} and -20% m^{-1},
   (b) g = 15% m^{-1}, 0% m^{-1} and -15% m^{-1},
   (c) g = 10% m^{-1}, 0% m^{-1} and -10% m^{-1},
   (d) g = 5% m^{-1}, 0% m^{-1} and -5% m^{-1}.
7. Power-law fits for λ_L=532 nm.
   (a) g = 20% m^{-1}, 0% m^{-1}, and -20% m^{-1}
   (b) g = 15% m^{-1}, 0% m^{-1} and -15% m^{-1},
   (c) g = 10% m^{-1}, 0% m^{-1} and -10% m^{-1},
   (d) g = 5% m^{-1}, 0% m^{-1} and -5% m^{-1}.
8. Power-law fits curve and computational points on a linear plot for g= +20% m^{-1}, 0% m^{-1} and -20% m^{-1}.
   (a) for λ_L=480 nm,
   (b) for λ_L=532 nm.
9. Power-law fitting parameters A and B vs. gradient g.
   (a) for λ_L=480 nm,
   (b) for λ_L=532 nm.

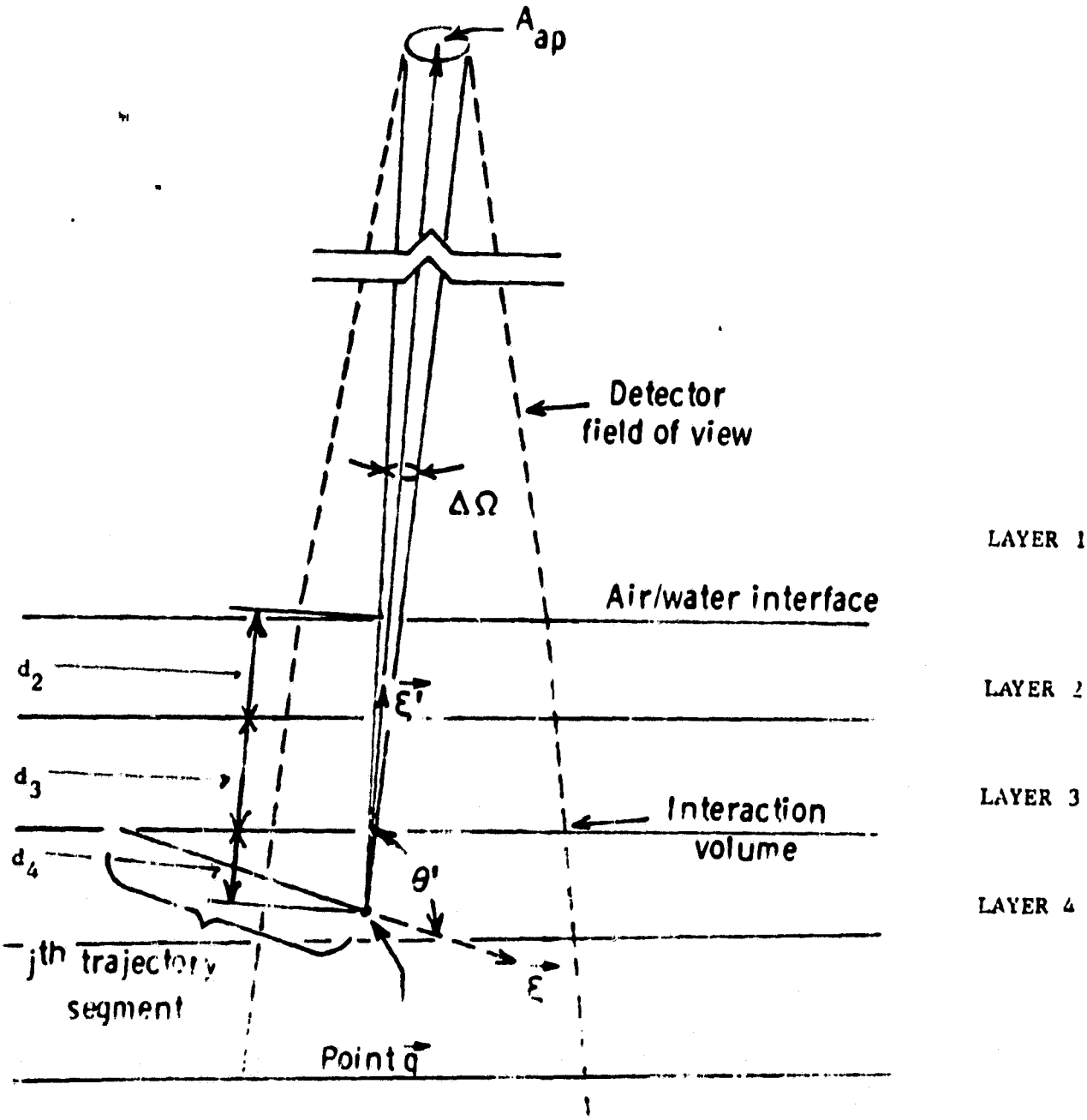

FIGURE 1

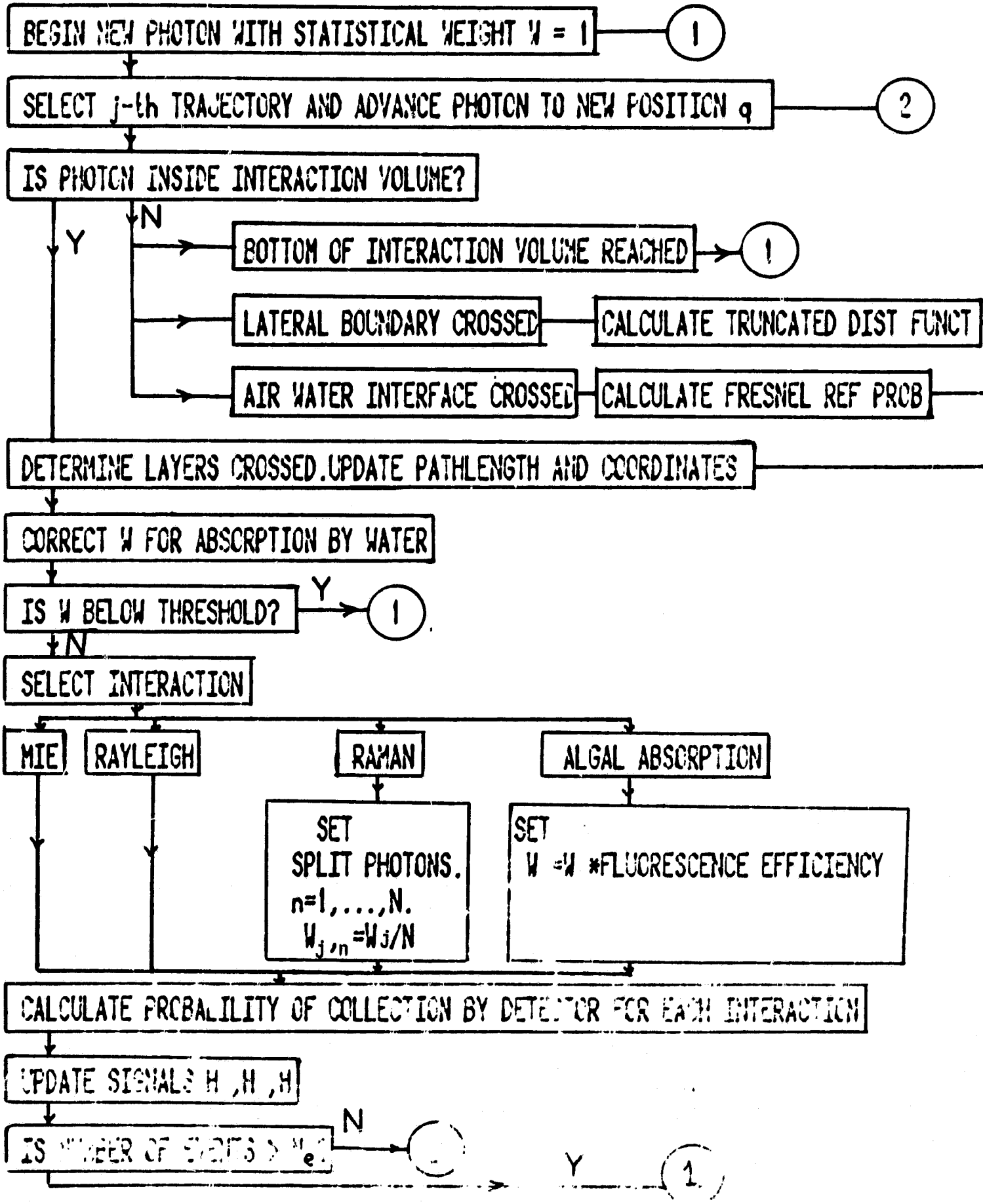

FIGURE 2

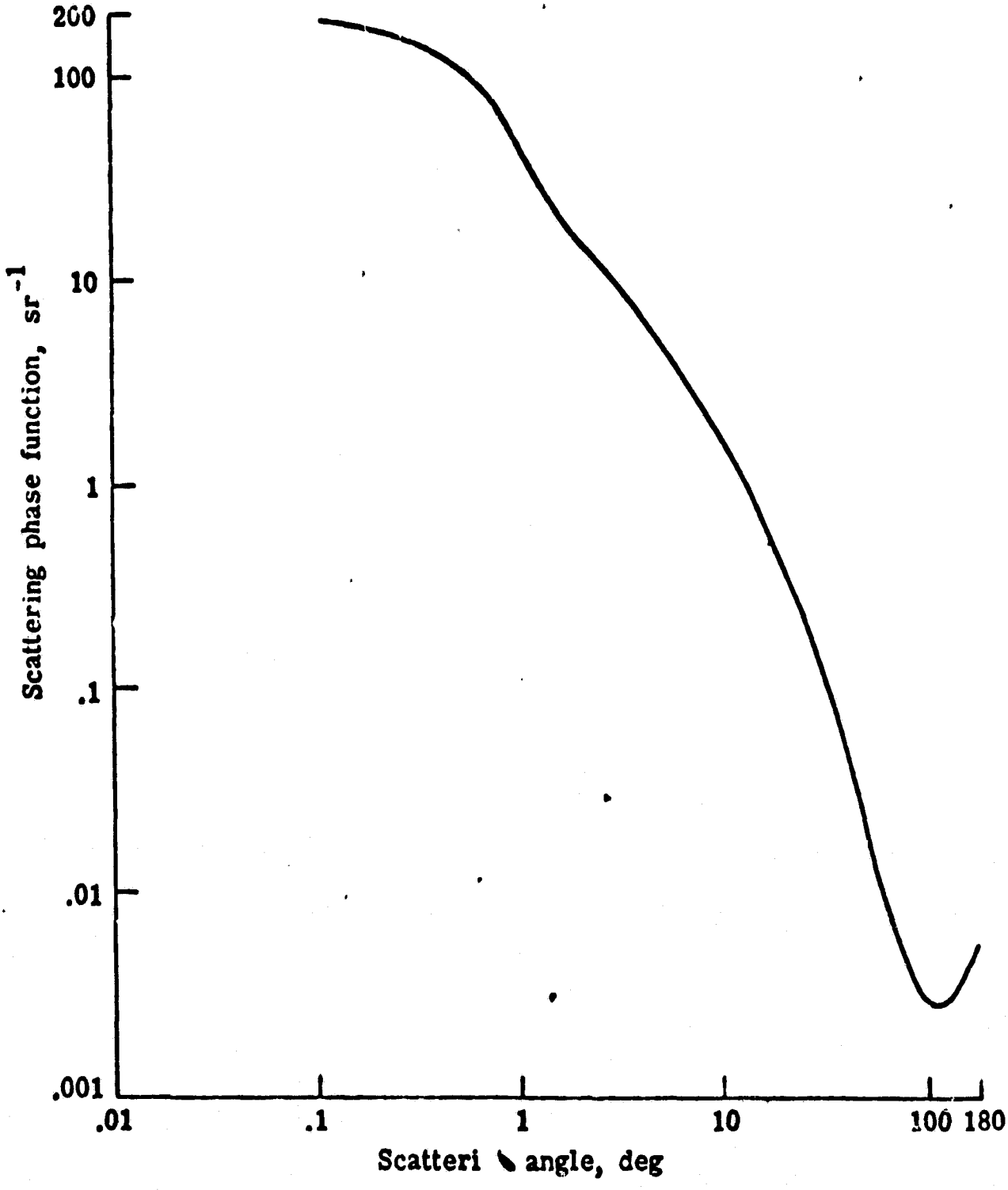

FIGURE 3

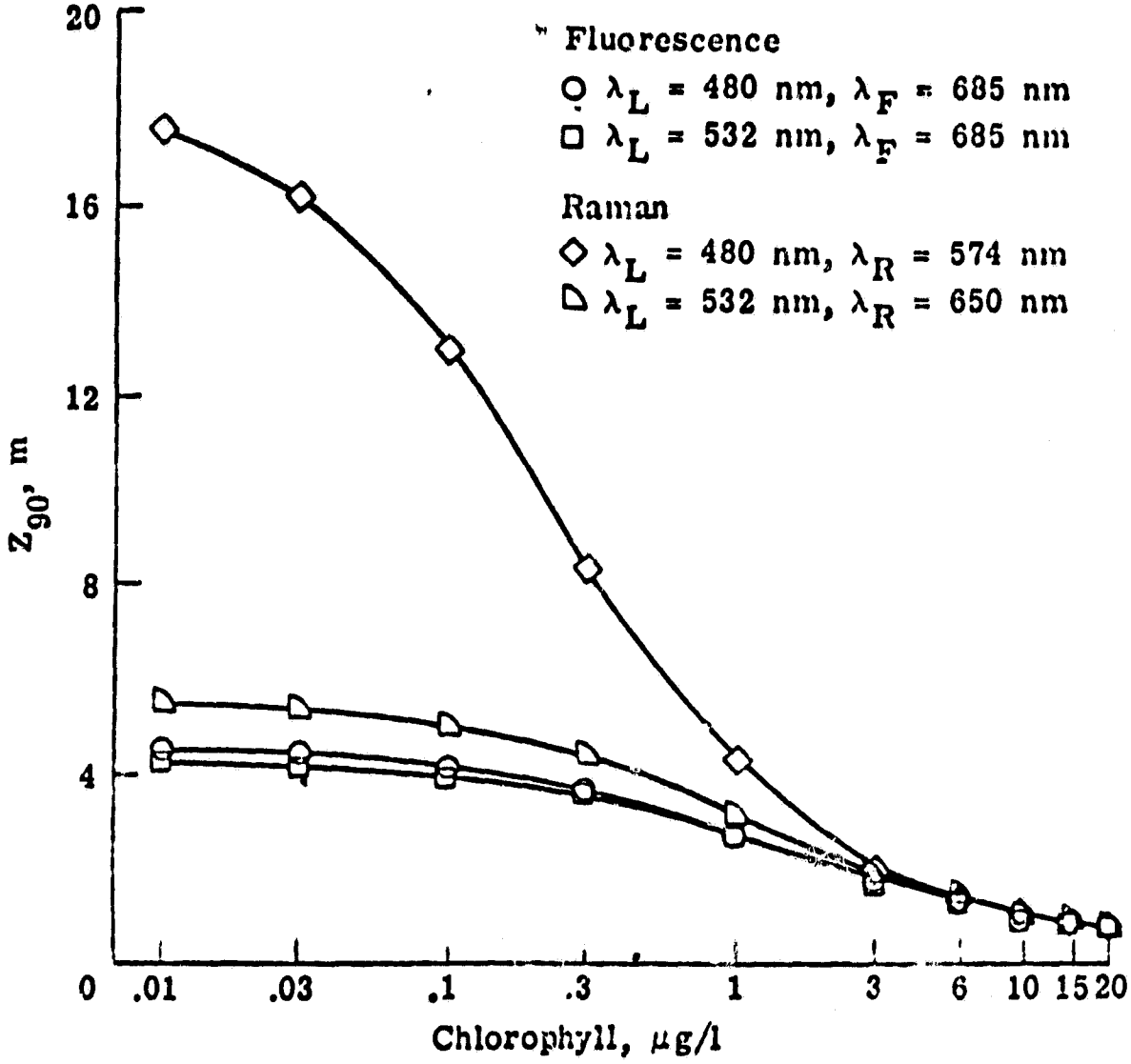

FIGURE 4

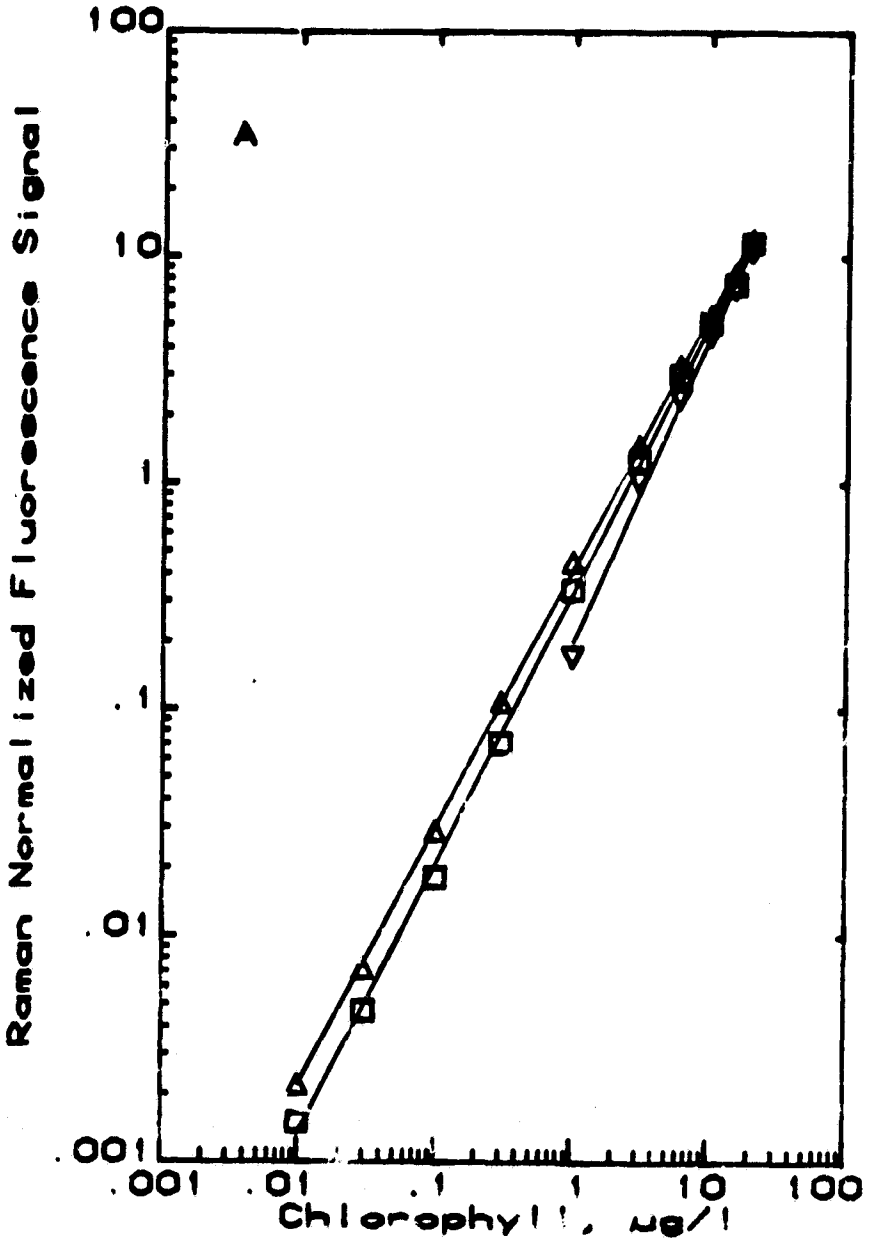

FIGURE 5(a)

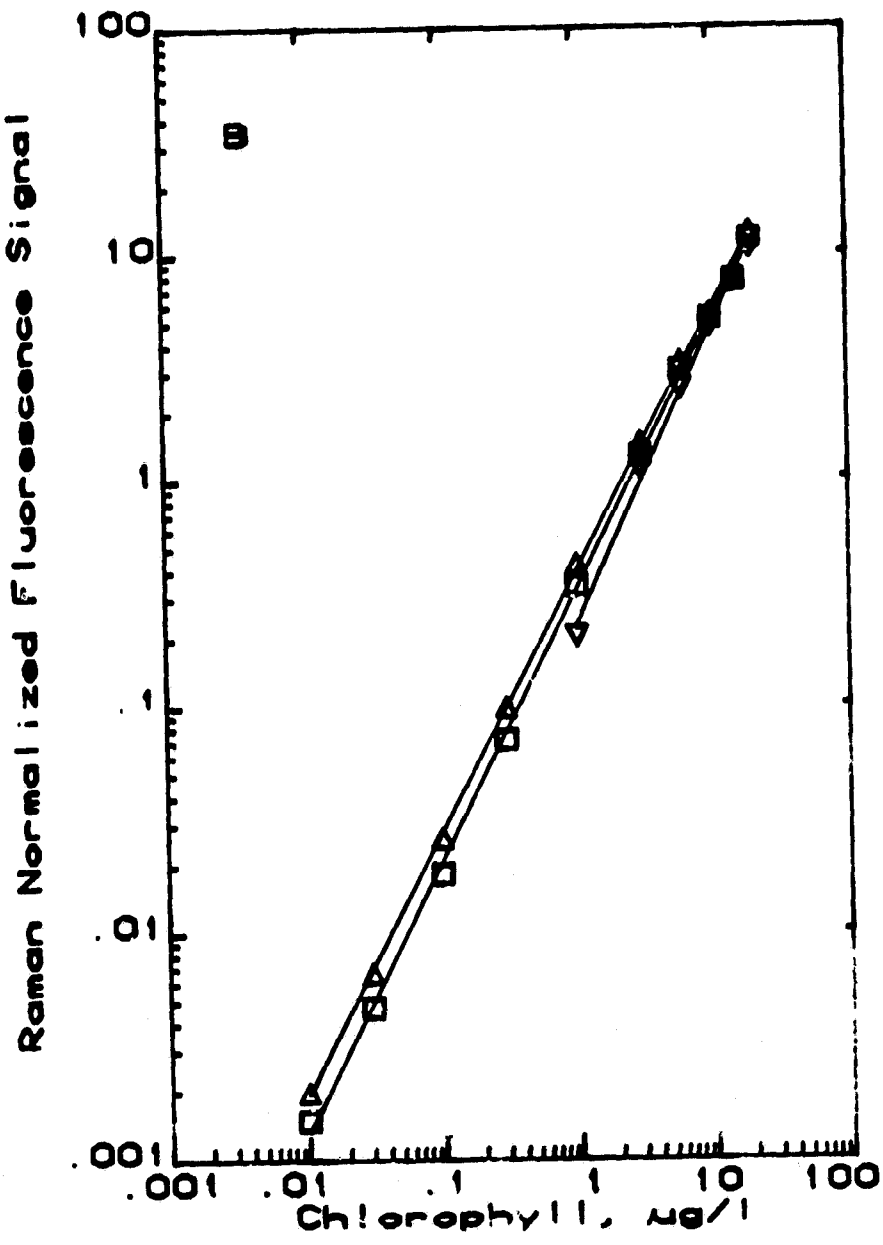

FIGURE 5(b)

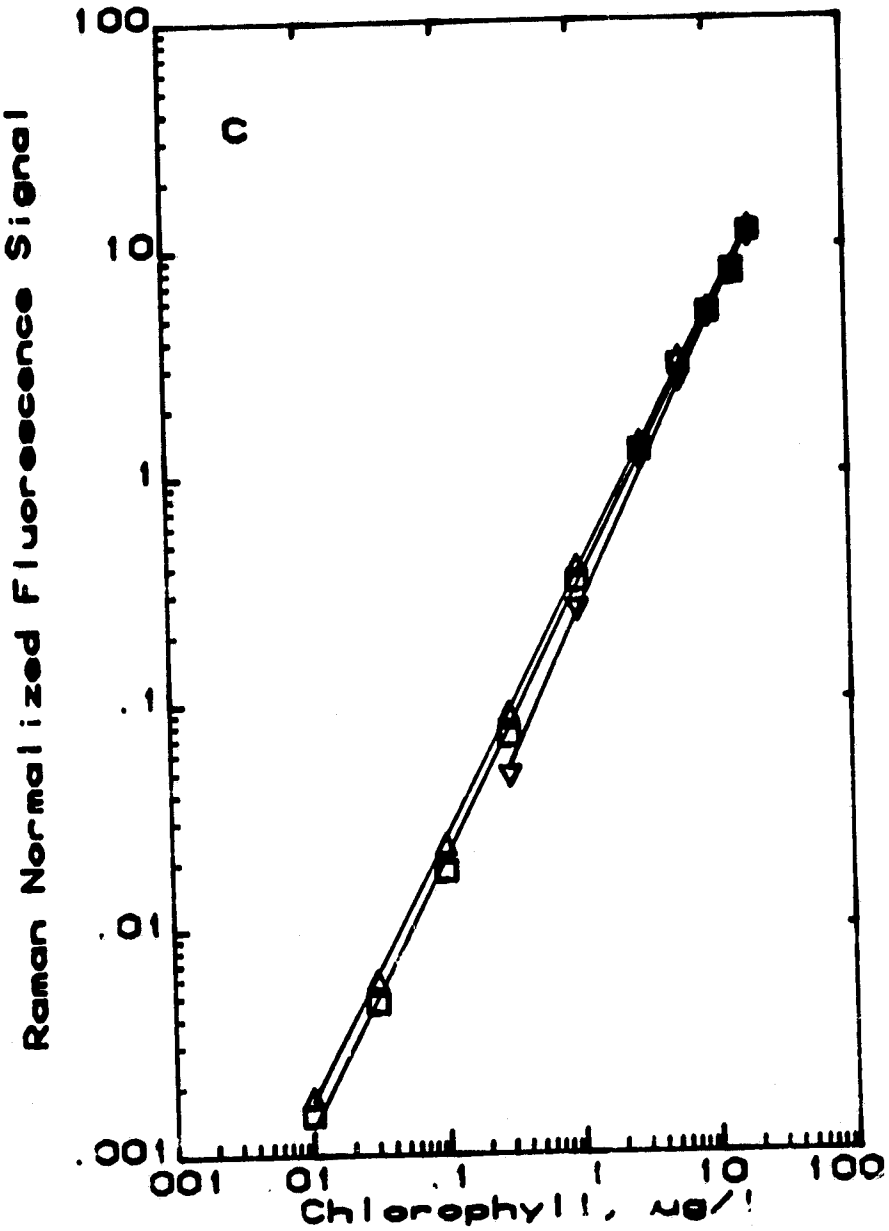

FIGURE 5(c)

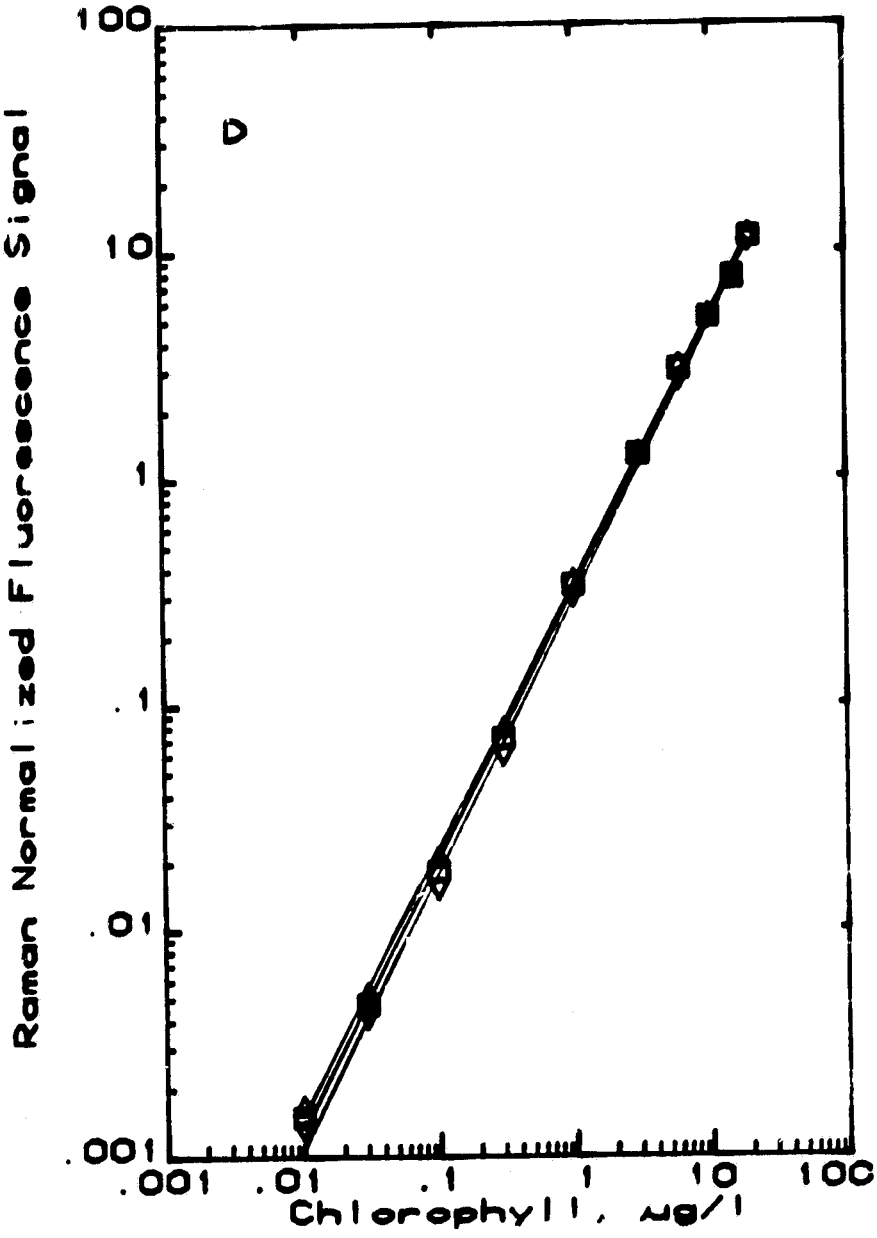

FIGURE 5(d)

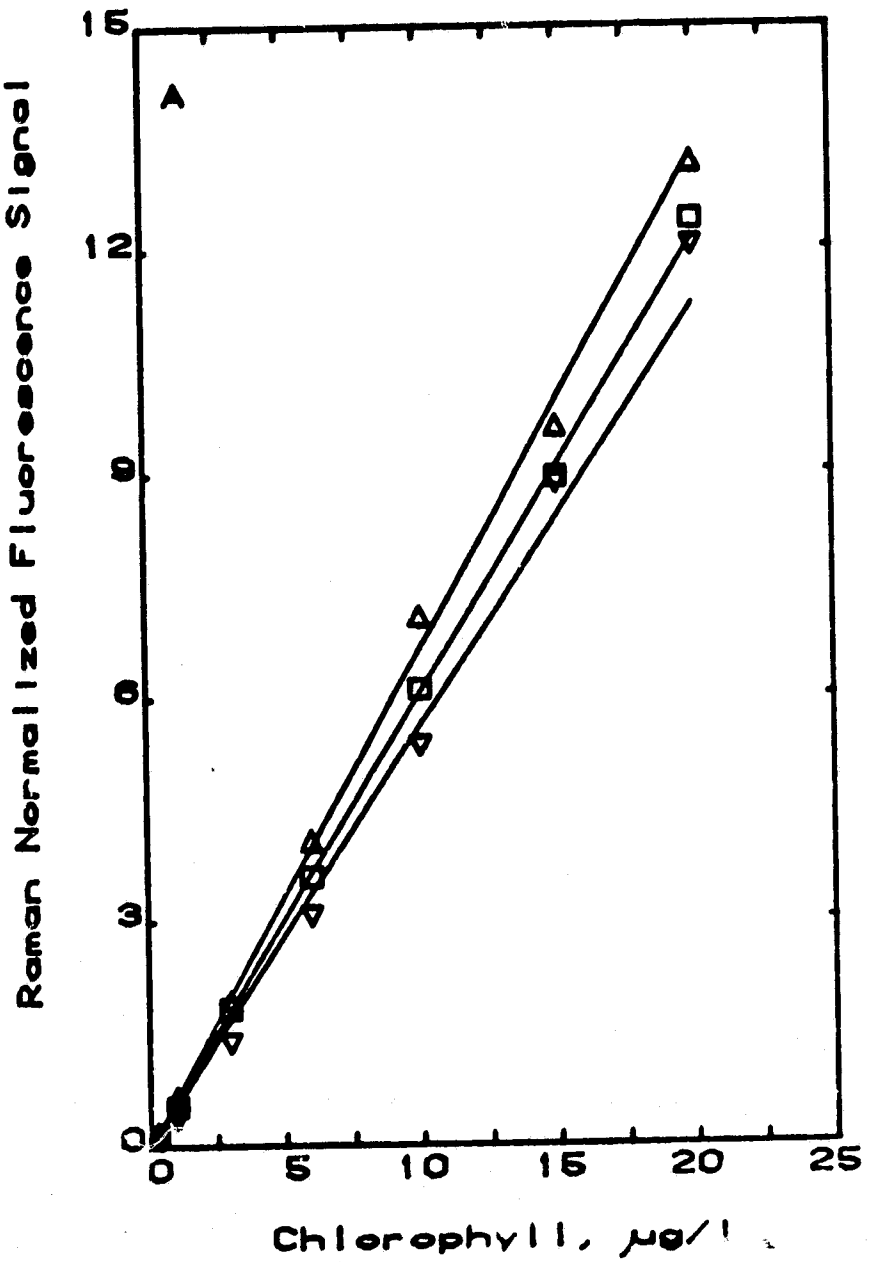

FIGURE 6(a)

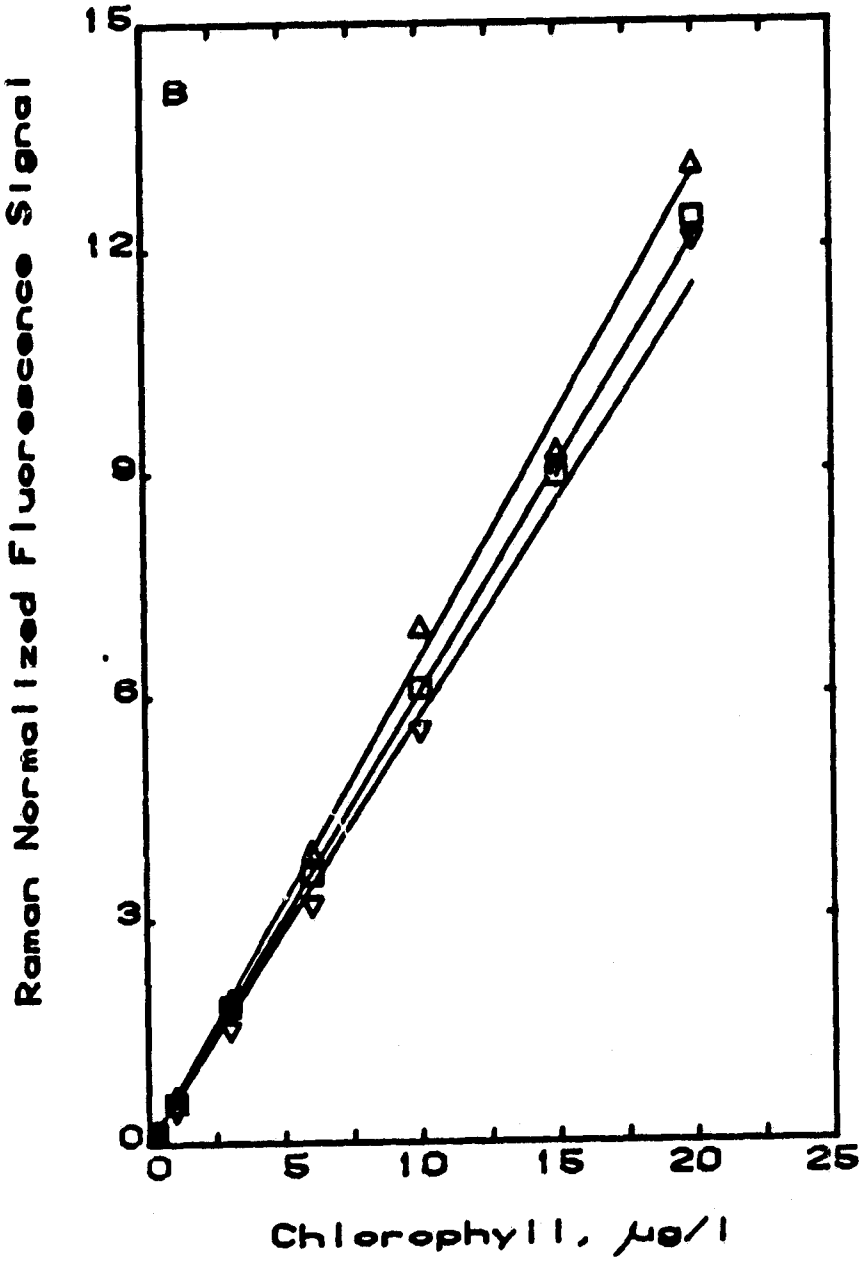

FIGURE 6(b)

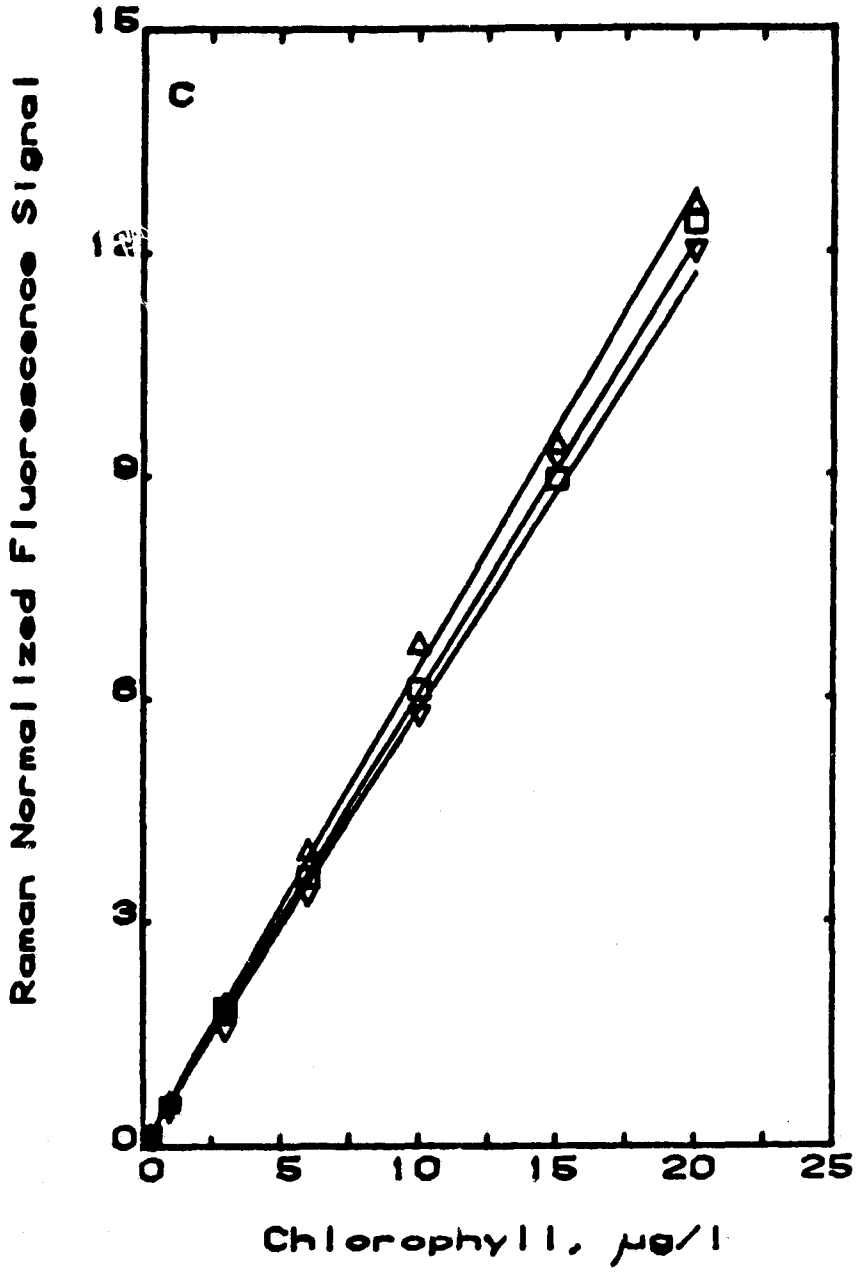

FIGURE 6(c)

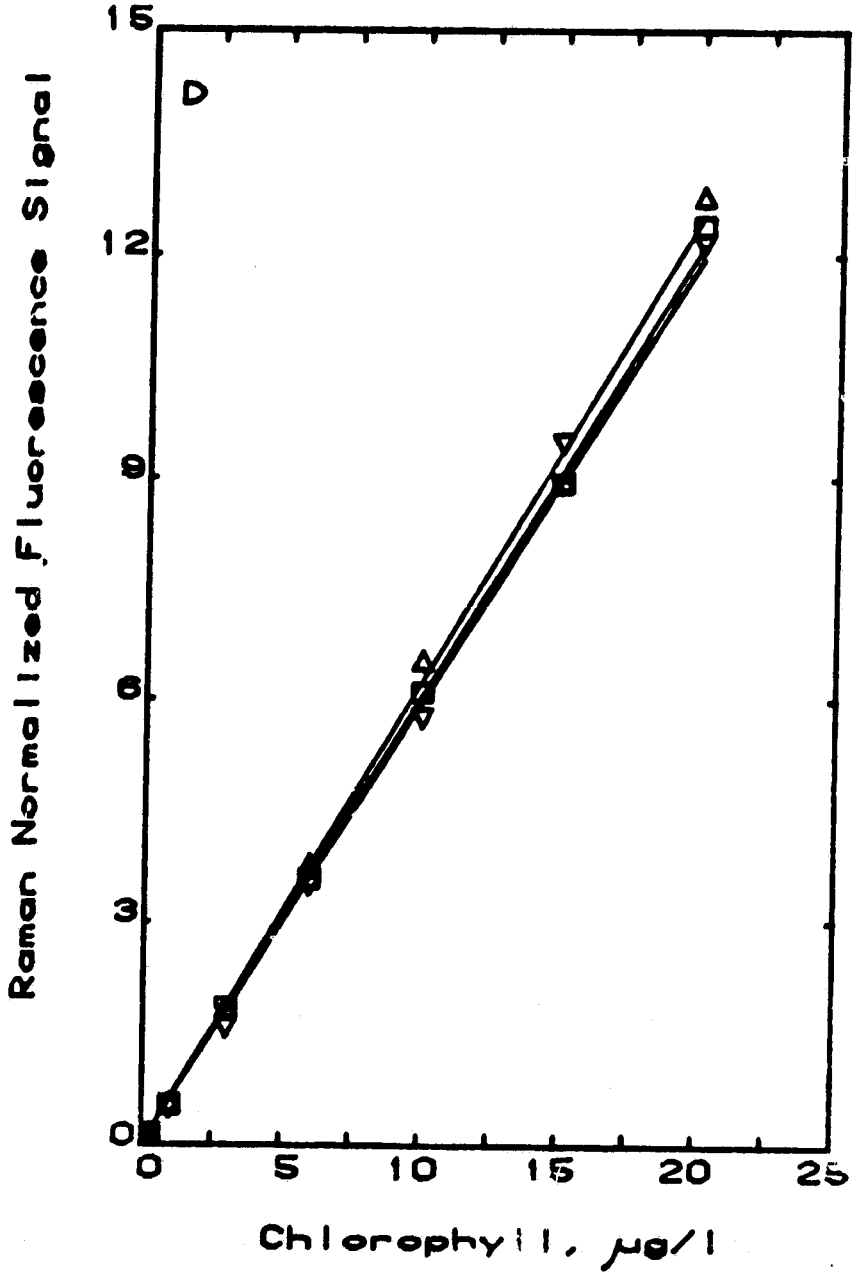

FIGURE 6(d)

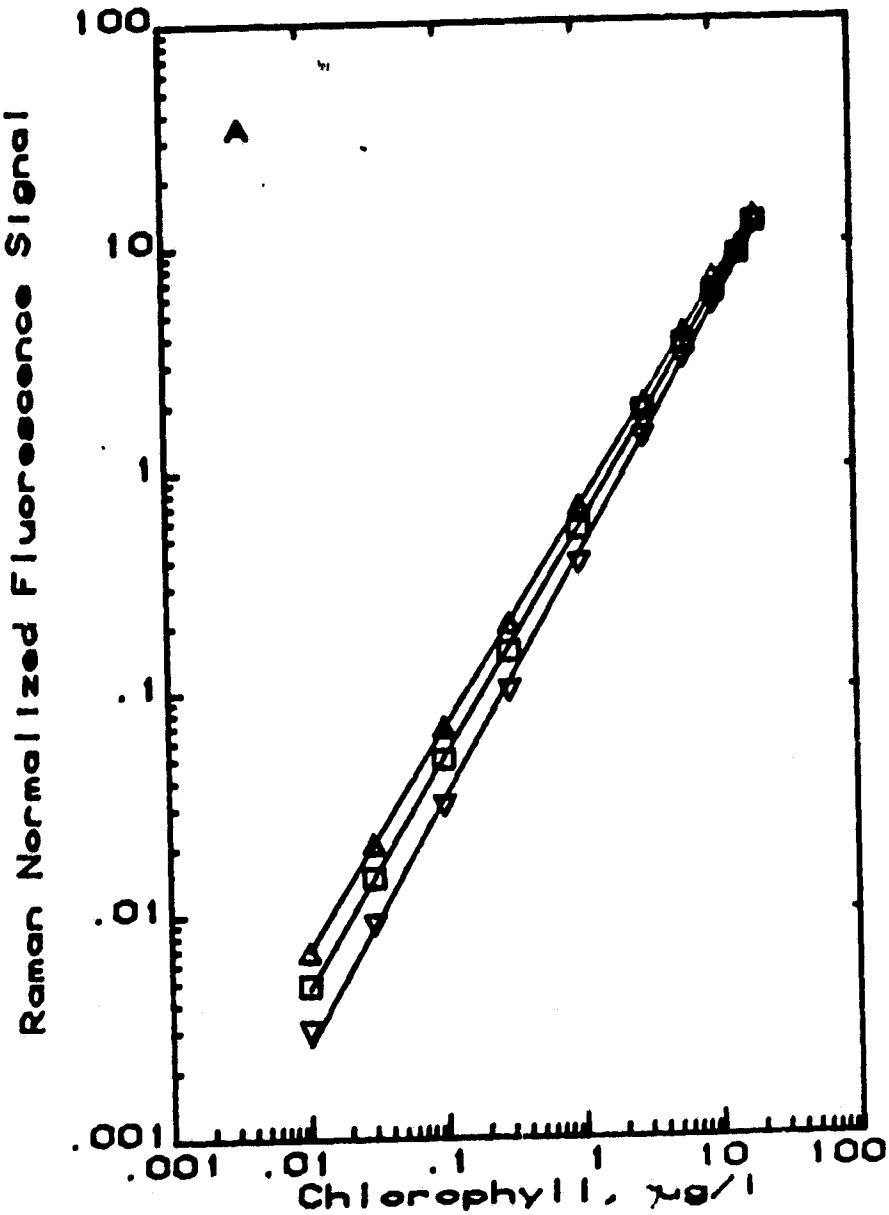

FIGURE 7(a)

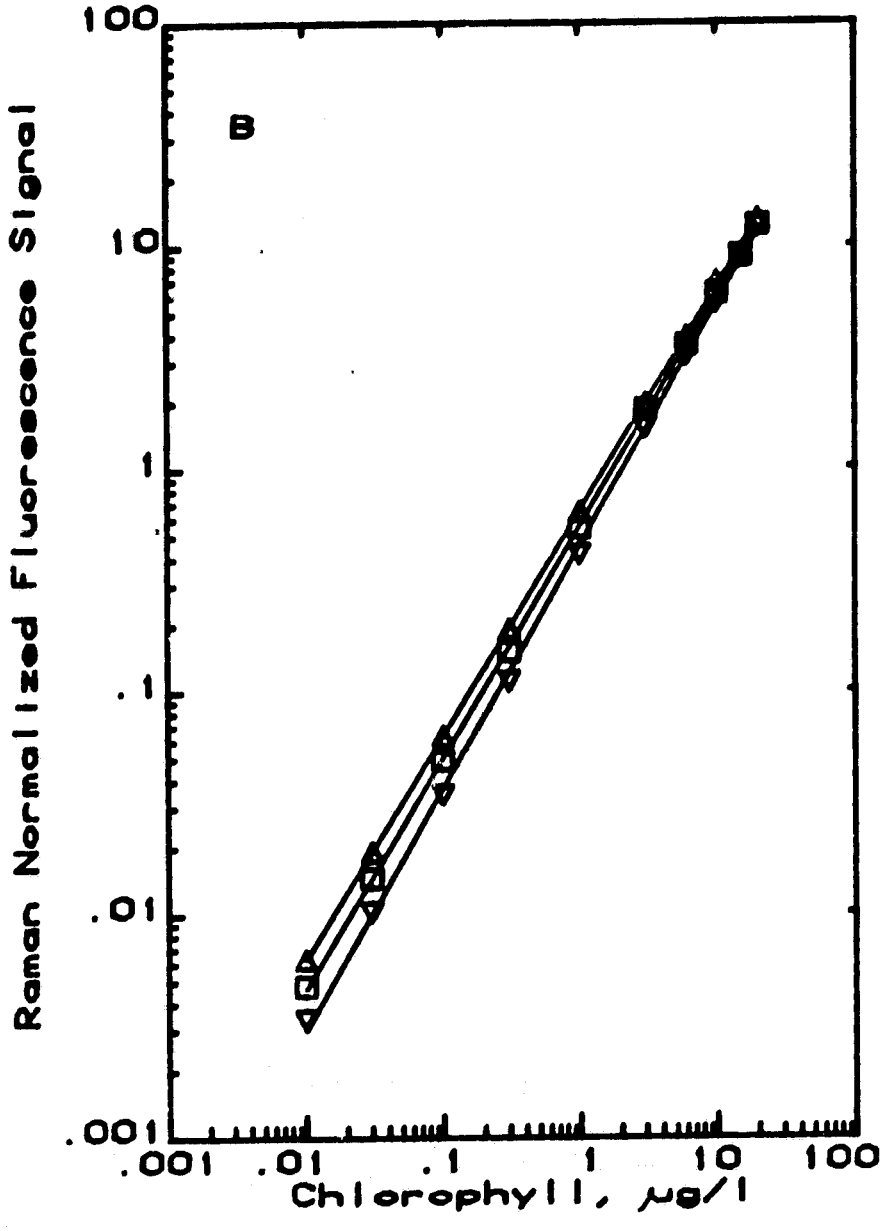

FIGURE 7(b)

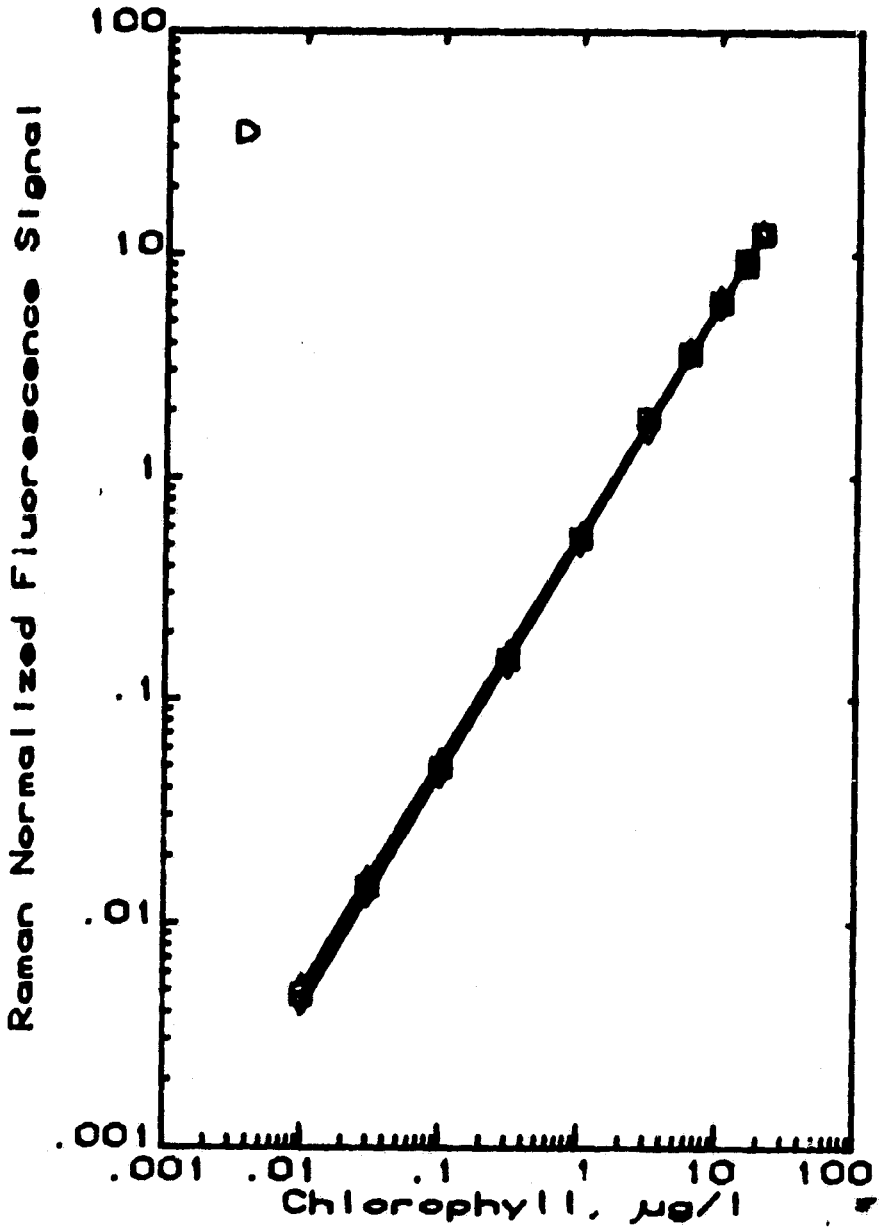

FIGURE 7(A)

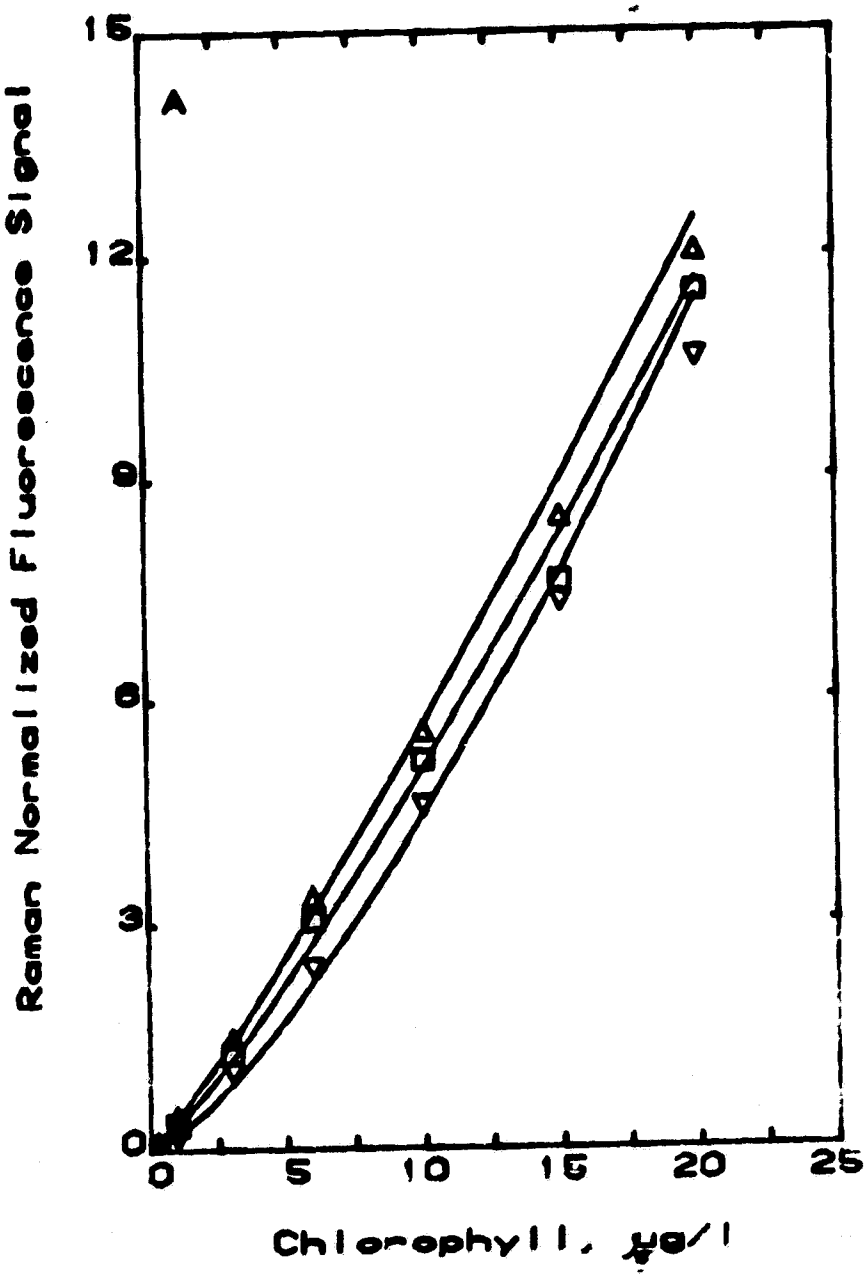

FIGURE 8(a)

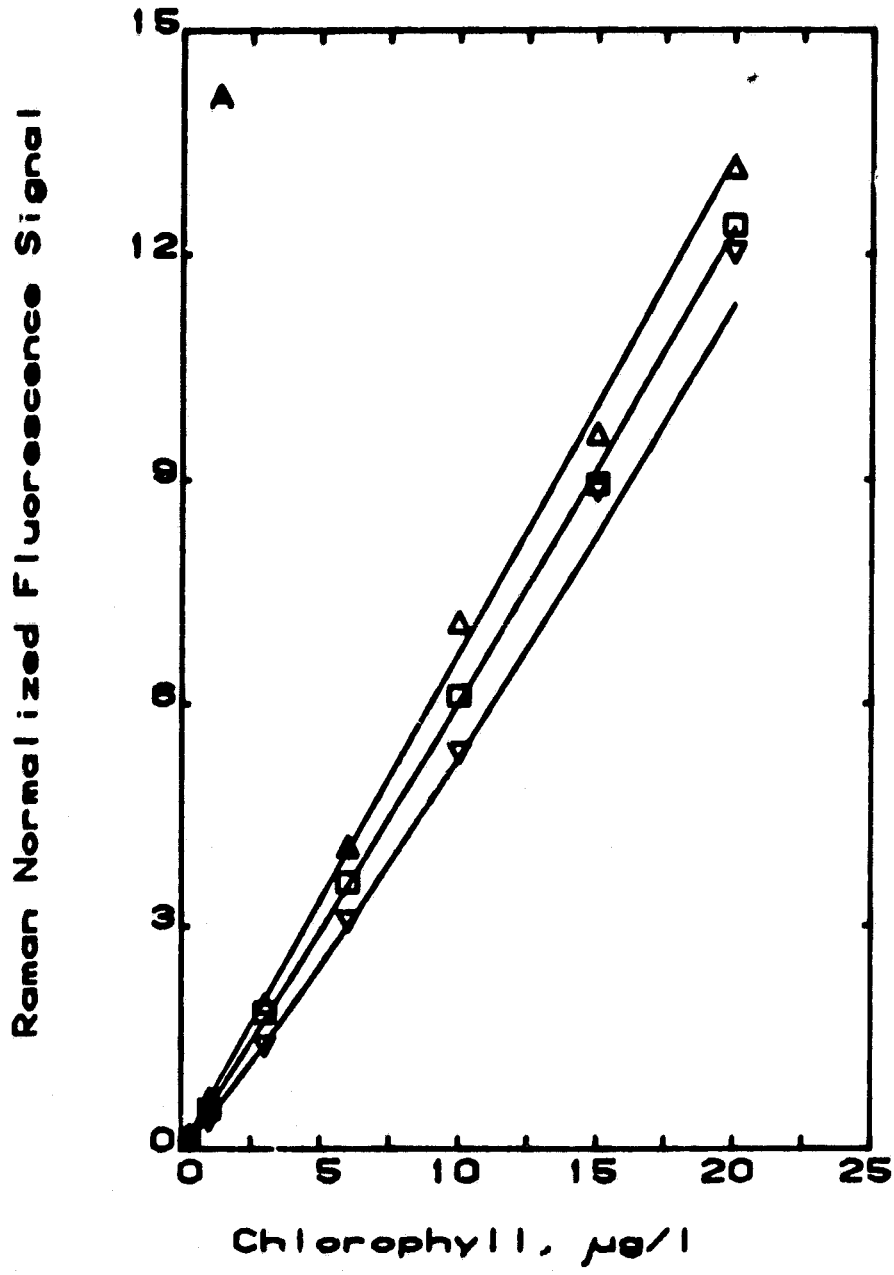

FIGURE 8(b)

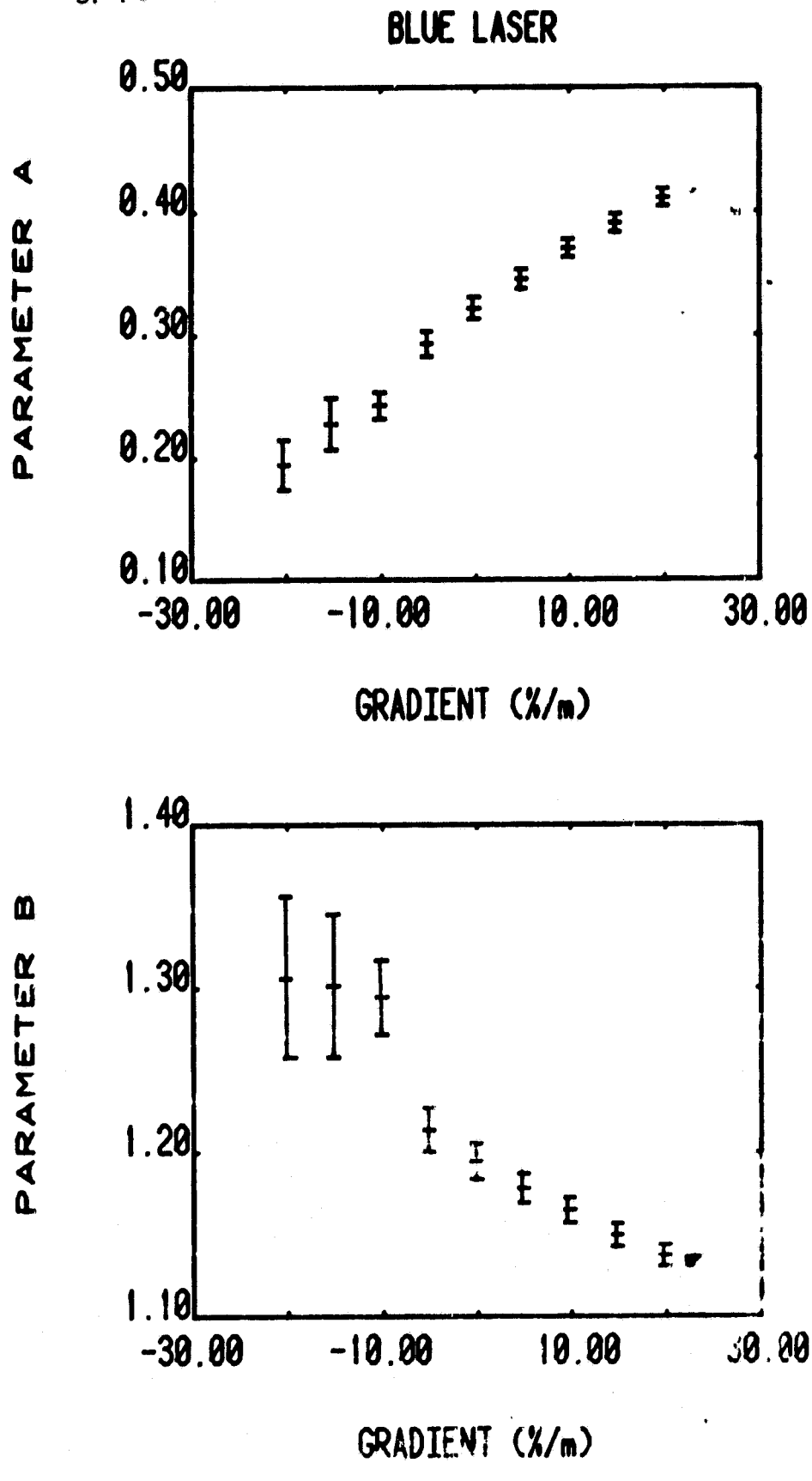

FIGURE 9(a)

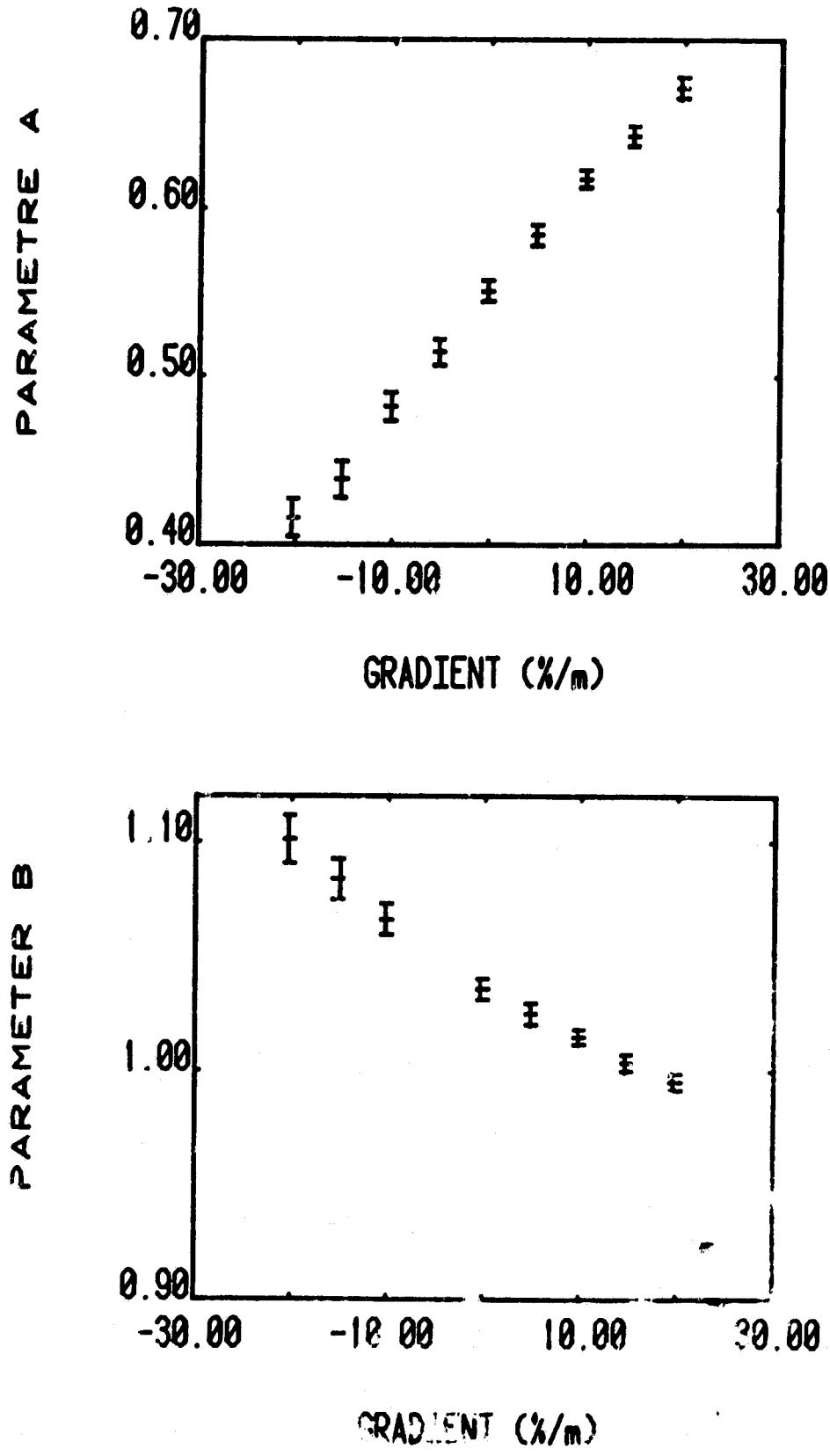

FIGURE 9(b)

Appendix I: Comparison of Stratified SALMON and Original Homogeneous Models

The original homogeneous SALMON model is operative on the NASA LaRC Cyber computer system. The stratified model is operative on the Hampton Institute VAX 11/780 computer system. The comparisons here are made for the zero gradient case for blue laser.

VAX 11/780 AT HAMPTON INSTITUTE

C (μs/1)	H_L	σ_L	H_R	σ_R	H_F	σ_F	N	T
0.01	0.1214E-07	0.9869E-10	0.3010E-08	0.2748E-10	0.4447E-11	0.7575E-13	30.	0.2181
0.03	0.1119E-07	0.2117E-09	0.2824E-08	0.2749E-10	0.1316E-10	0.1909E-12	32.	0.2277
0.10	0.9235E-08	0.2579E-09	0.2348E-08	0.4305E-10	0.4259E-10	0.5743E-12	41.	0.3066
0.30	0.7889E-08	0.2648E-09	0.1648E-08	0.3479E-10	0.1170E-09	0.2638E-11	40.	0.3651
1.00	0.7692E-08	0.3130E-09	0.9381E-09	0.3329E-10	0.3191E-09	0.1186E-10	54.	0.4219
3.00	0.9159E-08	0.4365E-09	0.5138E-09	0.2212E-10	0.6525E-09	0.1569E-10	77.	0.6243
6.00	0.9790E-08	0.4354E-09	0.3305E-09	0.1810E-10	0.1006E-08	0.4117E-10	61.	0.6804
10.00	0.1132E-07	0.5261E-09	0.2458E-09	0.1470E-10	0.1275E-08	0.4479E-10	73.	0.7163
15.00	0.1209E-07	0.5439E-09	0.2006E-09	0.1368E-10	0.1545E-08	0.4884E-10	71.	0.7883
20.00	0.1334E-07	0.6416E-09	0.1514E-09	0.1051E-10	0.1766E-08	0.5178E-10	98.	0.8644

CDC CYBER 175 MODEL AT NASA LRC
CPUTIME=VECP/5.0

C (μs/1)	H_L	σ_L	H_R	σ_R	H_F	σ_F	N	T
0.03	0.1123E-07	0.2205E-09	0.2845E-08	0.8214E-10	0.1268E-10	0.3229E-12	30.	0.1536
0.1	0.9280E-08	0.4329E-09	0.2349E-08	0.5808E-10	0.4046E-10	0.1102E-11	30.	0.1237
0.3	0.7562E-08	0.3323E-09	0.1652E-08	0.7991E-10	0.1115E-09	0.3461E-12	34.	0.2775
1.0	0.7835E-08	0.7279E-09	0.9349E-09	0.6734E-10	0.2990E-09	0.8864E-11	13.	0.1849
3.0	0.8219E-08	0.6844E-09	0.5352E-09	0.5858E-10	0.6546E-09	0.3755E-10	36.	0.3150
6.0	0.1052E-07	0.1039E-08	0.3527E-09	0.4253E-10	0.9859E-09	0.5785E-10	67.	0.3405
10.0	0.1162E-07	0.1149E-08	0.2434E-09	0.2344E-10	0.1290E-08	0.9020E-10	80.	0.2340
15.0	0.1236E-07	0.1227E-08	0.1905E-09	0.2168E-10	0.1550E-08	0.1240E-09	74.	0.2486
20.0	0.1356E-07	0.1346E-08	0.1641E-09	0.2073E-10	0.1816E-08	0.1212E-09	96.	0.2937

N is number of samples
T IS CPU time per sample in minutes